Available online at www.sciencedirect.com
SCIENCE DIRECT®
Ore Geology Reviews 24 (2004) 7–44
ORE GEOLOGY REVIEWS
www.elsevier.com/locate/oregeorev

Geology, composition, and genesis of the Sukhoi Log noble metals deposit, Russia

Vadim V. Distler[a,*], Marina A. Yudovskaya[a], Gennady L. Mitrofanov[b], Vsevolod Yu. Prokof'ev[a], Erick N. Lishnevskii[a]

[a] *Institute of Geology of Ore Deposits, Mineralogy, Petrography and Geochemistry (IGEM) Russian Academy of Science (RAS), Staromonethy, 35 Moscow 109017, Russia*
[b] *East-Siberian Scientific Research Institute of Geology, Geophysics and Mineral Resources, Irkutsk, Russia*

Abstract

With resources estimated at 1100 t Au at an average grade of 2.45 g/t, the black shale-hosted Sukhoi Log noble metals deposit is the largest concentration of gold in Russia. The Au mineralization and associated platinum group element (PGE) mineralization of the Sukhoi Log deposit is controlled by a tectonic zone along the axis of an overturned anticline located in metamorphosed carbon-bearing Upper Proterozoic sedimentary rocks. Organic compounds have been carbonatized by hydrothermal fluids. The centro-symmetric zoning of the mineralization is typical of infiltration metasomatism whereas disseminated and veinlet gold deposits accompanied by a quartz, carbonate, and pyrite assemblage were superimposed on sedimentary rocks. Nearly 90 minerals occur at Sukhoi Log including native metals, intermetallic alloys, sulfosalts, phosphates, tungstates, and oxides. Native gold is the main one mineral, but calaverite, hessite, petzite, and krennerite also occur. PGE mineralization is located on the periphery of the gold mineralization in the form of native platinum, Pt–Cu–Fe metal alloys, sperrylite, and cooperite. The mineral assemblage also includes native Fe, Cr, Cu, Ni, Sn, W, Ti, and Te, as well as alloys of these metals. The ore-forming process involved fluid temperatures of 130–395 °C, pressures of 0.2–2.4 kbar, and salt concentrations of 3.7–9.5 wt.% NaCl equiv.

Mineralogical, geochemical, and geophysical studies were used to develop a three-stage genetic model of the deposit involving deposition of terrigenous and carbon-bearing terrigenous-carbonate rocks in an intraplate rift about 800 Ma followed by regional metamorphism at 520 Ma culminating in the development of palingenetic granites and hydrothermal fluids transporting contrasting assemblages of elements—(Cr, Ni, Ti, Pt + Pd) and (Sn, W, Mo, Zr, Au, Ag, Zn + Pb)—at 320 Ma.

Keywords: Gold; Platinum; Black shale; Hydrothermal fluid; Fluid inclusion; Rare-earth elements

1. Introduction

The complexity and high economic value of ores hosted by carbonaceous black shale assemblages of the Earth's crust justify the intensive investigation that they have received (Coveney et al., 1992; Pašava, 1993; Gize, 1999). The Sukhoi Log noble metals deposit is the largest black shale-hosted deposit in Russia. Gold resources are currently estimated at 1100 t Au with an average grade of 2.45 ppm (Mitrofanov et al., 1994). The discovery of platinum mineralization (Distler et al., 1996) may be a key element in the

* Corresponding author. Fax: +7-95-230-21-79.
E-mail addresses: distler@igem.ru, maiya@igem.ru (V.V. Distler).

0169-1368/$ - see front matter © 2003 Elsevier B.V. All rights reserved.
doi:10.1016/j.oregeorev.2003.08.007

commercial viability of this deposit, if the problems with platinum recovery can be resolved.

The Sukhoi Log deposit is situated about 120 km north of Bodaibo in the Irkutsk region (Fig. 1) in the Lena gold bearing district which is the richest source of placer gold in Russia. Total placer gold production from the middle of the last century to the present of about 1500 t and the placers continue to be worked by Lena Gold and independent prospectors. The region is located within the Baikal-Patom Highland represented by peneplaned mountains to a 1200-m elevation. The period of continental erosion and denudation in this region has lasted from the Middle Paleozoic until the present day resulting in accumulation of up to 250 m of Phanerozoic placers in the Lena district containing up to 400 ppm Au (Vysotskii, 1933). The older alluvial and fluvial–glacial sands contain the highest-grade placers and are overlapped by lower-grade recent alluvial placers, partially formed by erosion of the older placers. The Sukhoi Log deposit, which does not crop out, is the only large lode gold deposit in this area. Thick auriferous quartz lodes with gold contents of up to 40 ppm located in rocks that overlie the Sukhoi Log deposit were mined in the area in the 1950–1960s. The basic framework for the geological structure of the deposit, the ore mineralogy, and gold distribution was determined by detailed studies in the 1970s (Mitrofanov et al., 1994; Buryak and Khmelevskaya, 1997).

This paper concentrates on the platinum mineralization in the Suhkoi Log deposit but also covers general questions about the nature of the deposit, the ore composition, and genesis.

Fig. 1. Location map of the Sukhoi Log deposit.

2. Geological setting

2.1. Regional geology and stratigraphy

The Sukhoi Log deposit is located within a complicated regional structure known as the Bodaibo synclinorium, corresponding geographically to the Baikal Platform Highland. The setting of the synclinorium is illustrated in Fig. 2. Early, Middle, and Late Riphean metasediments of the Bodaibo synclinorium unconformably overlie Archean–Proterozoic metamorphic rocks.

Lower Riphean stratigraphic divisions include the Purpol Formation, which consists of greenschist-facies conglomerates, sandstones and shales, and the Medvezhevsk Formation, which is composed of volcanogenic and volcano-terrigenous rocks. Andesite, andesite–basalts, and tuffs are intercalated with sandstones and conglomerates, and ferruginous quartzites.

The Middle Riphean begins with the Balaganakh Group, which is up to 2500 m thick, and consists mainly of terrigenous gravel–sand–siltstone sediments, succeeding calcareous sandstones and limestones. Middle and Late Riphean sedimentary rocks of the Nigry Group are divided into the Buzhuikhta, Ugokhan, Khomolkho, and Imnyakh Formations with a total thickness up to 1500 m, although intensive plastic deformation commonly results in lesser thicknesses.

The flysch of the Khomolkho Formation hosts all of the gold mineralization in the Sukhoi Log deposit. The silty and calcareous carbon-bearing shales contain abundant diagenetic sulfides.

Up to 2500 m of rhythmically interbedded sandstones, shales, carbonaceous shales, limestones, and sandstones of the Vendian Bodaibo Group terminate the Late Proterozoic sequences. Terrigenous and carbonaceous layers enriched in organic carbon are characteristic of the region. Carbon-bearing sediment deposition reached a maximum in the Middle and Late Riphean. The amount of organic matter increases from carbonate to sandstone to siltstone to pelite, following the normal sequence of sedimentary succession (Ronov and Migdisov, 1971).

A foreland basin associated with an intercontinental rift system probably developed in the region during the Middle and Late Riphean although no evidence

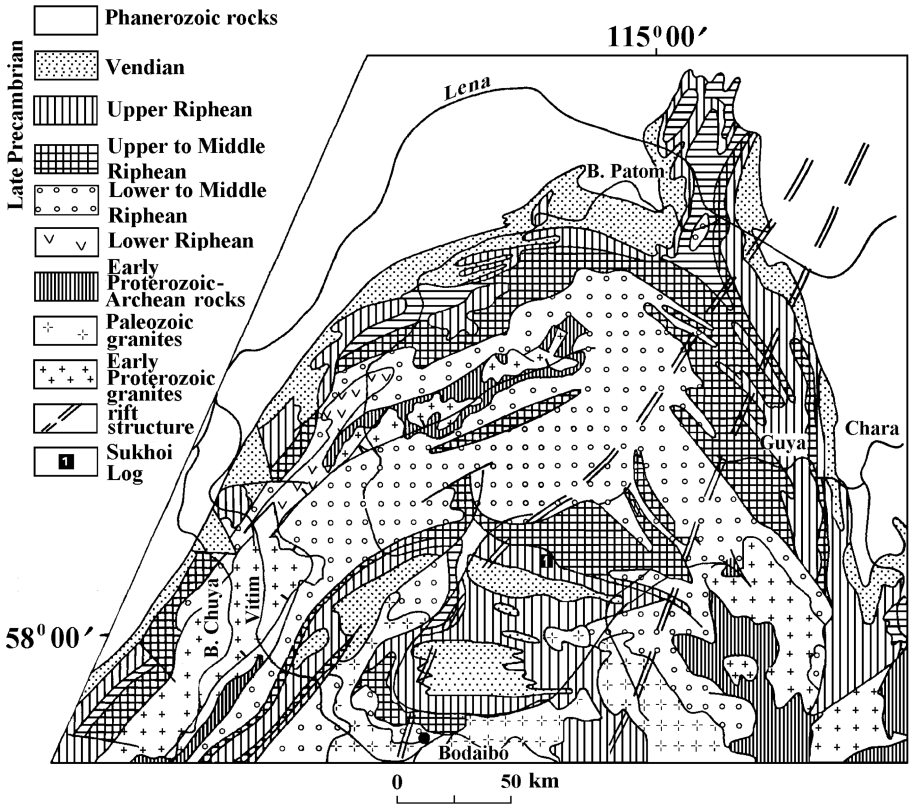

Fig. 2. Geological map of the Sukhoi Log ore district (modified by Mitrofanov et al., 1994).

remains of oceanic crust. Terrigenous carbonaceous rocks formed under conditions of a continental margin sea basin. Minor amounts of Lower Riphean volcanics are intercalated with coarse-grained clastics and ferriferous quartzites. At the same time, ophiolitic associations, including ultramafic rocks and tholeiitic volcanics, formed nearby and developed during the Early Paleozoic Bodaibo synclinorium. The complexity of the structure of the synclinorium is due to a combination of shallow folds with disrupted low angle fault zones (Rundqist et al., 1992).

The central part of the synclinorium has been metamorphosed to the biotite subfacies of the greenschist facies. Peripheral rocks have experienced epidote–amphibolite and amphibolite facies regional metamorphism associated with formation of granite–gneiss domes and palingenetic granitoid plutons (Buryak and Khmelevskaya, 1997).

Magmatic rocks related to the Middle Paleozoic Konkuder-Mamakan Complex (Rundqist et al., 1992) occur near Sukhoi Log. The Konstantinovsk massif (Fig. 3) occurs 6 km southwest of the deposit. On the periphery of the Bodaibo synclinorium, large Paleozoic granite intrusions, such as the Dzhegdakar massif, are exposed.

2.2. Geophysical data and deep structure of region

Regional geophysical exploration including seismic, magnetic, electric, and gravimetric prospecting has been carried out in the Baikal-Patom Highland (Mishenkin et al., 1975). Three seismic profiles were taken across the region in a north–south direction, in order to trace the Mohorovicic (Moho) discontinuity, which occurs at a depth of 35–37 km. The boundary velocity on the mantle surface averages 7.6–7.8 km/s. Using reflected wave data from all profiles, the average velocity of the Earth's crust was determined as 6.4 ± 0.1 km/s. The Moho abruptly plunges on the northern part of the synclinorium to a depth of 45–47

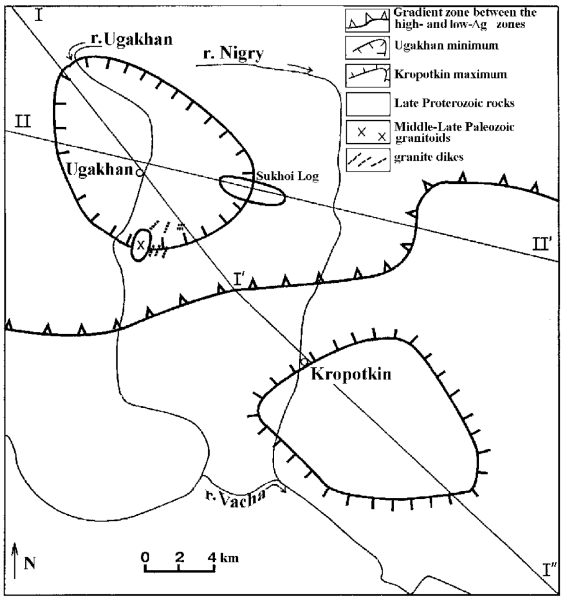

Fig. 3. Position of the Sukhoi Log deposit with respect to geophysical and structural features.

km, where the boundary velocity reaches 8.4–8.8 km/s.

South of Bodaibo in the northern part of the Baikalian Barguzin-Vitim fold system, coinciding with the Baikal rift zone, the Moho gently dips to a depth of 41–44 km where the boundary velocity on the mantle's surface approximates that of the synclinorium averaging 7.7–7.9 km/s.

The anomalously low boundary velocity of the Bodaibo synclinorium and the southern part of the Baikal rift zone may represent poor compression of the upper mantle. This may reflect tectonic–magmatic activation that took place discontinuously from the Middle Paleozoic in the Bodaibo synclinorium to the Cenozoic in the Baikal rift zone.

The southern part of the synclinorium is located within a high-gravity zone whereas the northern part contains the Ugakhan gravity low (Fig. 3), the Konstantinovsk granite massif, and Sukhoi Log deposit. The Kropotkin local gravity high is found 10 km southeast of Sukhoi Log (Laverov et al., 2000a).

The Ugakhan low reflects rocks lower in density than the host Late Proterozoic sedimentary sequences that have an average density of 2.68–2.70 g/cm^3. Among the rocks of the Bodaibo synclinorium, only normal granites have a lower density ($\rho = 2.60$ g/cm^3). The Konkuder-Mamakan granite bodies are traced by subisometric negative anomalies and may be represented by the partially exposed Dzhegdakar granite massif. Similar Δg lows produced by partially exposed or hidden deep-seated granite bodies are typical for the Transbaikalian region and define the endogenous ore districts hosting tin, tungsten, molybdenum, and gold deposits. The Ugakhan Δg low probably reflects a hidden granite body, termed the Ugakhan Massif, with a density of 2.60 g/cm^3. Roof depth of the Ugakhan granite pluton was determined on the basis of the gravitation field variations. In the absence of direct data on rock density, a roof depth of 3–3.2 km was calculated from interrelated profiles. In plan view, the Ugakhan pluton has an oval shape and closely reflects the configuration of the Ugakhan local Δg low outlined by density-based gravimetric modelling underlying about 110 km^2 to a thickness as high as 6 km (Figs. 4 and 5).

The enormous Muruntau gold–platinum deposit in Uzbekistan occurs in a geological–geophysical setting similar to that of the Sukhoi Log deposit (Khamrabaev et al., 1995). For example, the Muruntau deposit is confined to the marginal part of a closed gravity low caused by hidden granite pluton, which has been the borehole that ran 290 m entirely through granite. The granites which make up the pluton have $\rho = 2.61$ g/cm^3, a lower density relative to the host metasedimentary rocks of 0.07–0.08 g/cm^3, and close to the parameters of the Sukhoi Log area.

Gravimetric modelling showed that the basement of this area mainly consists of rocks with $\rho = 2.80$ g/cm^3 that are interpreted as Archean metamorphic and mafic metavolcanic rocks. The Kropotkin Δg high corresponds to a subisometric body with $\rho = 2.94$ g/cm^3, located within this basement that probably consist of serpentinite.

The Kropotkin maximum is part of a continuous band of linear positive anomalies and beaded Δg highs, which can be traced over more than 2000 km along the southern margin of the Siberian platform (Fig. 6). This band ranges up to about 50 km in width and marks the conjunction of the Aldan shield and Stanovik fold system on the east, and then bends northward, cuts the Bodaibo synclinorium, and extends along Lake Baikal to the southwest. According to Alakshin and Pismennyi (1988), the zone

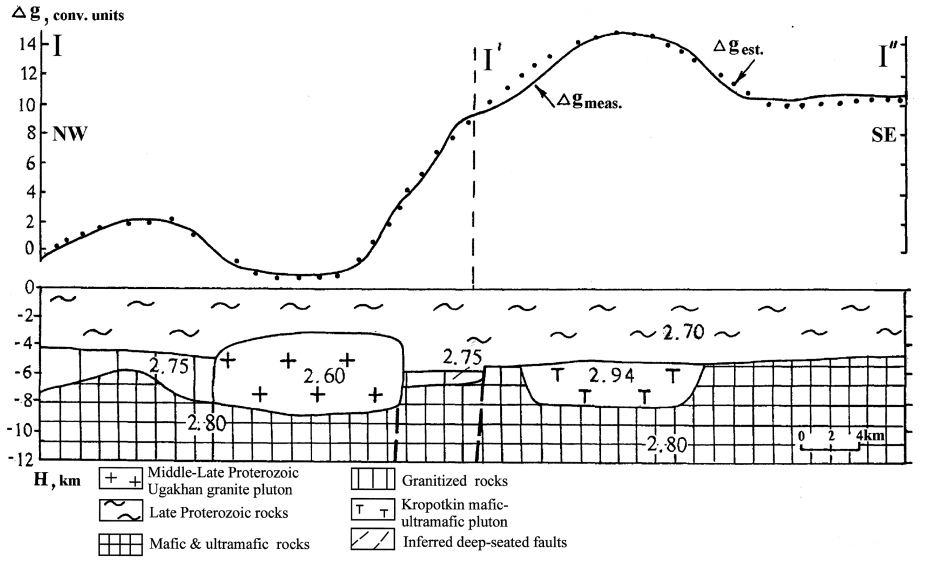

Fig. 4. Schematic deep-seated geological–geophysical profile along the I–I′–I″ profile. The numbers on the section show the density used for calculation (g/cm^3); curves indicate: Δg_{meas} is measured (initial) gravity; Δg_{est} is estimated gravity corresponding to given section.

corresponds to the partially hidden marginal mafic–ultramafic belt of the Siberian platform. On the surface, the high-density bodies responsible for the anomalies are Archean and Early Proterozoic ultramafics, gabbroids, and mafic–ultramafic amphibolites and schists. Significant bedrock platinum occurrences were found within such rocks in the conjunction zone of the Aldan shield and Stanovik fold system. Associated gold placers contain angular platinum group element (PGE) grains. Based on extrapolation of these occurrences northwest along the described system of Δg anomalies, the platinum and gold mineralization of the Sukhoi Log deposit may be connected with the Early Precambrian mafic–ultramafic rocks, which are

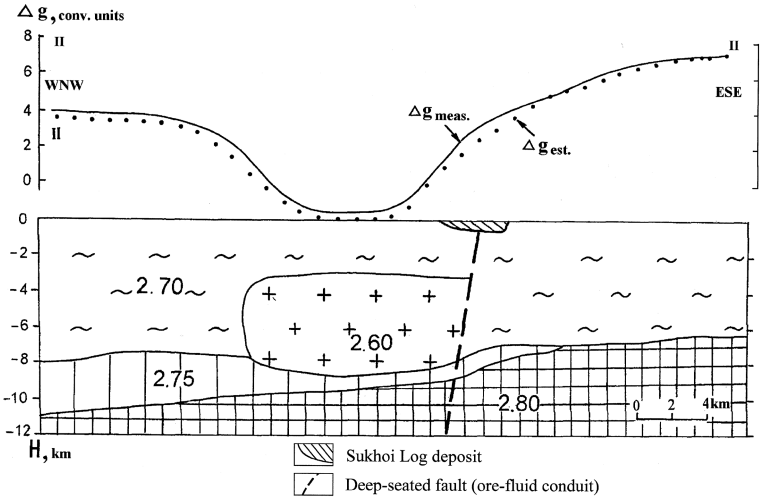

Fig. 5. Schematic deep-seated geological–geophysical section across the unexposed Ugakhan granite pluton and Sukhoi Log deposit along the II–II′ profile. For other symbols, see Fig. 4.

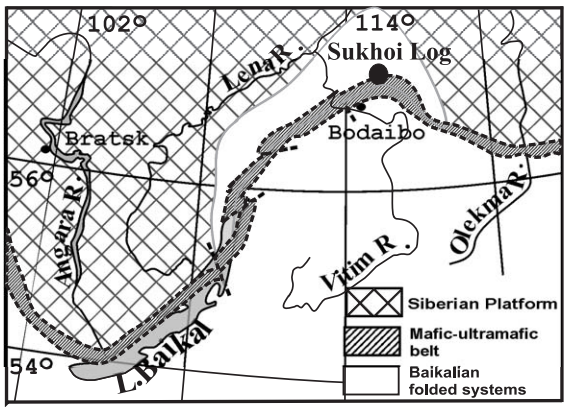

Fig. 6. The mafic–ultramafic marginal belt along the southern boundary of the Siberian craton.

characterized by high gold and platinum background values. Within the low-gravity zone, the basement roof is calculated to be at a depth of 5–9 km and includes an upper stratum with $\rho = 2.75$ g/cm^3 (Fig. 6).

2.3. Structural geology

The Sukhoi Log deposit is located on the axis of an overturned anticline (Fig. 7) whose bedding dips west at angles of 5–20°. Its axial surface plunges gently and its trend changes from east–west to northwest at angles of 30–40 °C. The northern normal flank dips 15–30°; the southern overturned flank dips 30–50°. A fault zone is present in the axial part of fold where thicknesses of the host rocks are considerably decreased and deformed. An intraformational overthrust zone is found on the southern flank of the field.

Host rocks belong to the Middle–Late Riphean flyschoid complex and are most strongly enriched in carbon in the middle of the section. Alternating 0.1–3 m beds of carbonaceous and calcareous siltstones, argillites, shales, and sandstones are characteristic of the sections.

2.4. Mineralization

The most intensely mineralized zones of the deposit lack sharp, visible geological boundaries, but their delineation was made on the basis of several criteria (Fig. 8) including assays from half-core samples taken at 1-m intervals. The protore has a centrosymmetric zonation in section. Subzones differ in the amount of sulfides, intensity of mineralization and the morphology of quartz–sulfide segregations. The ex-

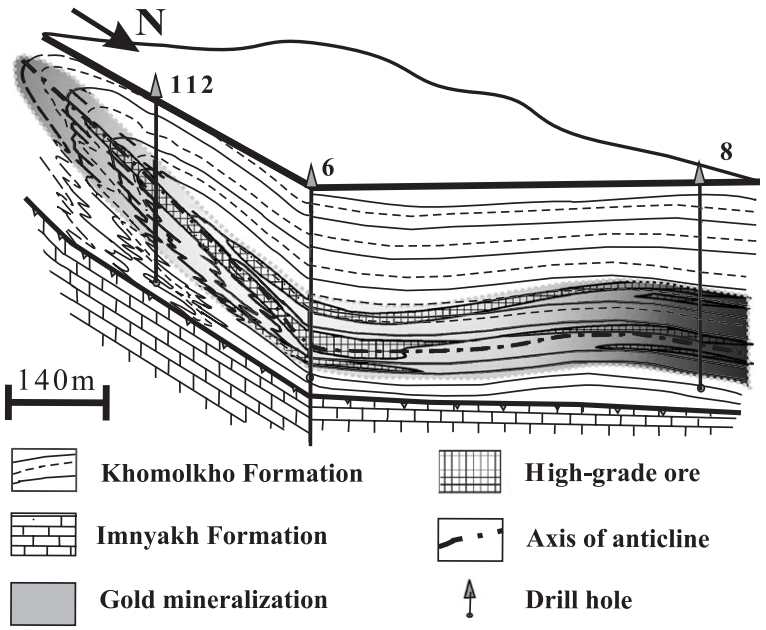

Fig. 7. Block-diagram illustrating geological structure and gold ore distribution of the Sukhoi Log deposit.

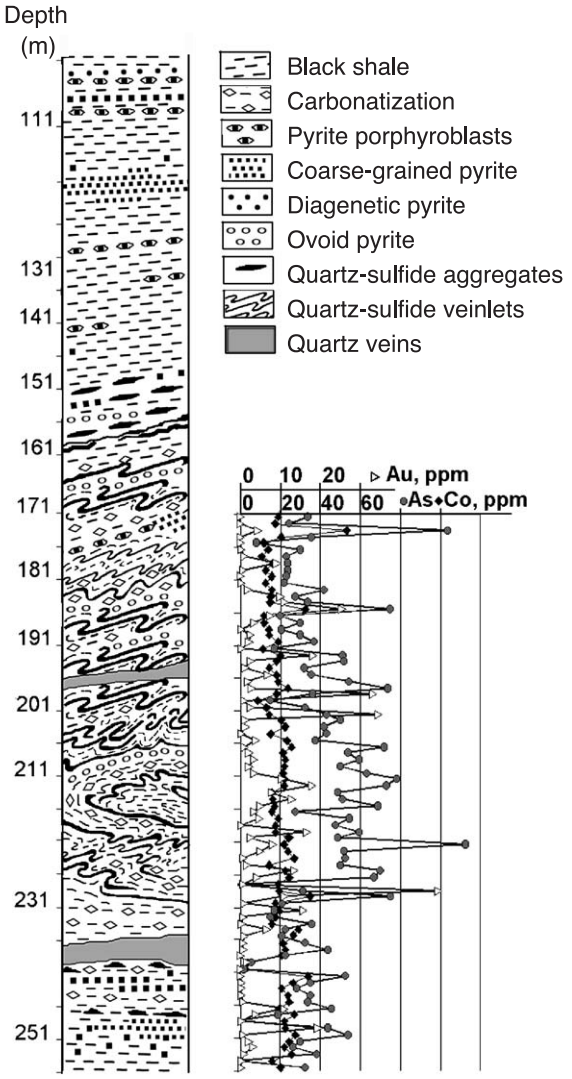

Fig. 8. Cross sections through orebody of the deposit on drill core 6 illustrating the main morphological types of quartz–sulfide mineralization and Au, As, and Co distribution.

terior subzone exhibits an increase in disseminated fine-grained pyrite, and large granoblastic pyrite as well as quartz–pyrite aggregates. The intermediate subzone contains few sulfides or quartz–sulfide veinlets. The central interior subzone occupies the axial part of the fold and contains abundant quartz–sulfide veinlets with complicated shapes inherited from folding and crinkling of the host shales.

Sulfide-poor quartz veins as much as 2 m thick occur together with the veinlet stockwork and disseminated mineralization especially at the tops of ore zones. Separate Au-poor quartz veins, which post-date mineralization are observed at deep levels of the deposit (up to 330–400 m from the surface).

The major gold reserves of the deposit are connected with veinlet-disseminated quartz–sulfide mineralization and can be subdivided into the following zones: supra-ore (upper exterior subzone), protore (intermediate and central subzones), and infra-ore (bottom exterior subzone).

The basic morphological types of gold mineralization are (Figs. 8, 9):

1. Interlayers and lenticles of diagenetic fine- and medium-grained pyrite;
2. Stratified impregnations of rounded ovoid pyrite;
3. Cleavable and foliated impregnations of fine-grained pyrite and pyrrhotite;
4. Large zonal metacrystals of pyrite with quartz margins;
5. Granoblastic pyrite aggregates;
6. Stratified and crossing quartz–sulfide stockwork veinlets up to 2–4 cm thickness.

Some of the above morphological types of mineralization (e.g. types 1–4) occur outside the deposit, but they are usually barren or contain only low-grade protore.

2.5. Metamorphic and metasomatic alteration

The carbon-bearing shales of the Khomolkho Formation are compositionally similar to the North American Shale Composite (NASC) (Taylor and McLennan, 1985), except that they contain elevated S (up to 20 wt.%), organic carbon (0.2–2.7 wt.%) and Na_2O (0.6–2.2 wt.%). The shales have been regionally metamorphosed to greenschist facies and are dominated by 30–35 vol.% quartz and 35–50 vol.% sericite, with a carbonate content from 5–30 vol.%. Minor minerals are rutile, magnetite, tourmaline, zircon, monazite, and albite.

The carbonaceous–terrigenous sediments enriched in organic matter were transformed into quartz–sericite shales containing rare Na-bearing muscovite, Fe-poor chlorite and epidote. Porphyroblastic disseminations of Fe–Mg carbonates were formed by meta-

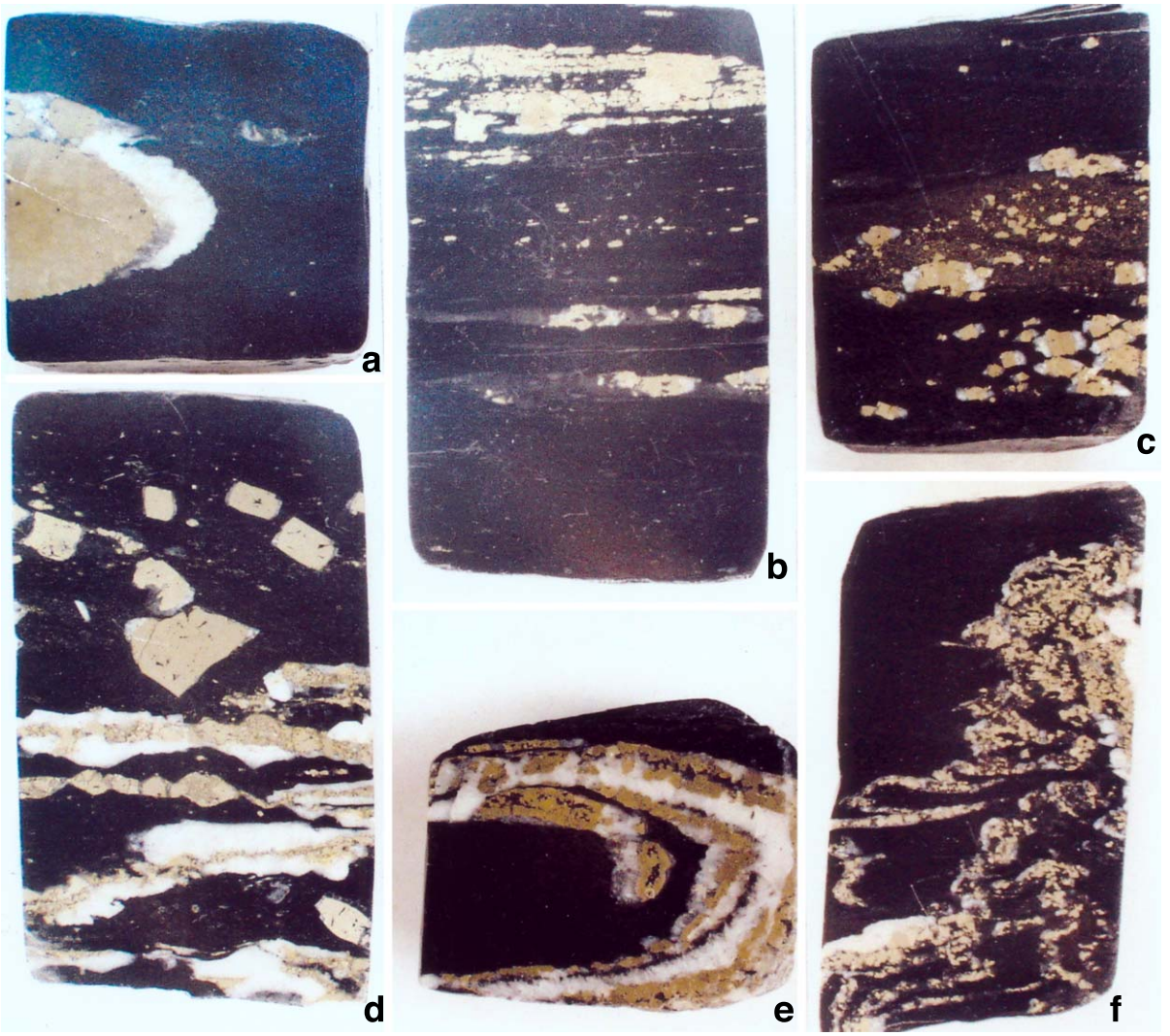

Fig. 9. Typical structures of platinum–gold ore of the Sukhoi Log deposit. Polished core sections (diameter of core is 6 cm). (a) Separate lenticular metagranoblastic quartz–pyrite aggregate; (b) cleavable oriented disseminated pyrite mineralization; (c) fine-grained and coarse-grained pyrite mineralization; (d) quartz–pyrite veinlets and porphyroblastic pyrite from the central part of orebody; (e, f) complexly folded of quartz–pyrite veinlets in the axial part of the Sukhoi Log anticline.

morphism of carbonaceous material and commonly contain carbonaceous inclusions.

3. Samples and analytical methods

3.1. Samples

More than 2700 m of drill core were studied including drill-core samples collected by the authors in 1994 and 1995 and specimens selected from 10 cores drilled in 1996 by the company, Lenzoloto. Material for polished sections and monomineralic samples was selected from each drill-core sample. Duplicates of powdered analytical samples were used for Au assays.

3.2. Analytical techniques

Mineral compositions of mineralized zones, metasomatites, and host rocks were studied by reflected

and transmitted light microscopy. The chemical compositions of micrograins of PGE, sulfides, sulfosalts, native elements, and monazites were determined using a Cameca MS-46 microprobe and a scanning electron microscope JSM-5300 with an Energy Dispersive Spectrometer (EDS) detector at the Institute of Geology of Ore Deposits, Mineralogy, Petrography and Geochemistry (IGEM), Russian Academy of Science (RAS), Moscow. Mineral compositions were determined at 20 kV accelerating voltage and 1-μm beam diameter.

Concentrations of gold and other metals were determined at the Chemical Laboratory IGEM RAS by instrumental neutron activation (INAA). The concentrations of rare-earth elements (REE) in bulk shale samples, quartz, carbonate, and sulfide concentrates were analyzed at the same laboratory using inductively coupled plasma–mass spectrometry (ICPMS). Analysis of element concentration in aqueous extracts from fluid inclusions was carried out at the Institute of Geochemistry, Siberian Branch RAS, by ICPMS.

Chemical determination of carbon, hydrogen, nitrogen, and sulfur (CHNS analysis) was conducted at the Laboratory of Analytical Chemistry, Vernadsky Institute of Geochemistry RAS. Phase composition of soluble organic matter was identified by chromato-mass-spectrometric method using Hewlett-Packard-5972 and Varian-3400. X-ray photoelectron spectroscopy and Auger spectroscopy data was also used for determination of the state of Au in carbonic matter.

Isotopic analysis of S and C was carried out by standard techniques in the Laboratory of Isotope Geochemistry and Geochronology, IGEM RAS and results were expressed relative to CDT, PDB, and SMOW standards, respectively.

3.3. Procedures of platinum group element study

The distributions PGE and coexisting native gold are the main focus of this paper. Particular attention was paid to the nugget effect and to the problem of accuracy, precision, and reproducibility of PGE analyses from organic carbon-bearing materials. It was unfortunately impossible to use fire assay analysis, one of the best methods of gold determination because reliable PGE determination in carbon-bearing rocks is hampered by severe analytical problems (Kucha, 1982; Van der Flier-Keller, 1991; Juvonen et al., 2000). Sources of overestimation can be controlled by application of traditional methods, previously used for sulfide ores, to analyze carbon-bearing rocks whose matrix can absorb many elements, in particular, uranium, thorium, REE, etc., by complex formation that makes PGE determination by INAA difficult. An additional problem is the formation of isotope ^{199}Au from gold-bearing materials since platinum content is measured on the same isotope by INAA.

The sorptive capacity of carbonaceous matter can be a source of inaccuracies during acid decomposition of samples. The insoluble remainder is excluded from the analysis together with noble metals sorbed on carbonaceous matter, which may result in erroneously low values. Formation of volatile carbonyl or carbonyl-chloride compounds in the process of analysis can cause loss of noble metals (Varshal et al., 1994).

In this study, we used several analytical methods for PGE determination. Each method was first tested using a standard sample prepared using wall rock with the addition of precisely fixed PGE amounts as salt solution. A series of comparative analyses was performed for the same weighted portions of more than 60 samples of mineralized rock using all methods, which allowed the determination of PGE concentrations in the reference sample with an error less than 30 relative percent. The analyses showed that all these methods yielded PGE concentrations from 0.0*n* to 10 ppm in specified samples. However, in some cases, the values obtained with different methods did not agree with each other. During further mass analysis of samples from the deposit, each sample was analyzed with two or three methods. In this study, we used analytical methods with chemical decomposition of samples, preconcentration of PGE on sorbents followed by determination of PGE concentrations with ICPMS, optical spectroscopy, spectrophotometry, neutron activation, as well as catalytic methods.

PGE contents in 2–5 g bulk samples, sulfide and ultra-heavy concentrates were determined by chemical analysis. Some aliquots of acid decomposition were also analyzed by ICPMS. Detection levels for chemical methods were (ppm) Pt—0.02, Pd—0.01, Rh—0.001, Ir—0.002, for ICPMS—Pt—0.005, Pd—0.005, Rh—0.0005, Ru—0.0002, Ir—0.0005.

Identification of PGE minerals, such as the 0.3–0.5 μm cooperite inclusion found in pyrite by Mitrofanov et al. (1994), constitutes the most reliable evidence of PGE mineralization at Sukhoi Log. The difficulty in finding platinum-bearing phases with optical microscopy led to attempts to look for PGE dissemination in sulfides or PGE in organic matter. Geological and experimental data demonstrate that some sulfides have significant isomorphous capacity toward platinum metals in solid solutions (Distler et al., 1988). The solid solution limits reach up to several tens of ppm of Rh, Ir, Ru, Os, and a few ppm of Pt in pyrrhotite, up to a few percent Pd, a few tens of percent of Rh and Ru, and several hundreds of ppm of Ir and Os in pentlandite. In minerals of the cobaltite–gersdorffite isomorphic series, up to a few tens of percent of Pd, Ru, Os, Ir, and a few percent of Pt are marked and up to a few percent of Rh, Ru, and Os in minerals of the Ni–As–S system.

Studies of pyrite from different genetic types of deposit with a proton microprobe (Cabri et al., 1985; Genkin et al., 1998; Distler et al., 1999) show that PGE concentrations in this mineral are less than a few tens of ppb. The highest concentrations of PGE are typical of high-temperature pyrrhotite, pentlandite, cobaltite–gersdorffite, and nickel arsenides. The lowest temperatures of crystallization of platinum-bearing sulfides and sulfarsenides are 450–550 °C, which corresponds to the amphibolite facies metamorphism.

According to Varshal et al. (1994), the noble metals are linked structurally and chemically with carbon in oxygen-bearing functional groups, so that the more abundant the oxygen-bearing functional groups are, the larger the amounts of noble metals that can be held in the organic matrix of the rocks. Organic matter commonly becomes graphitized during metamorphism.

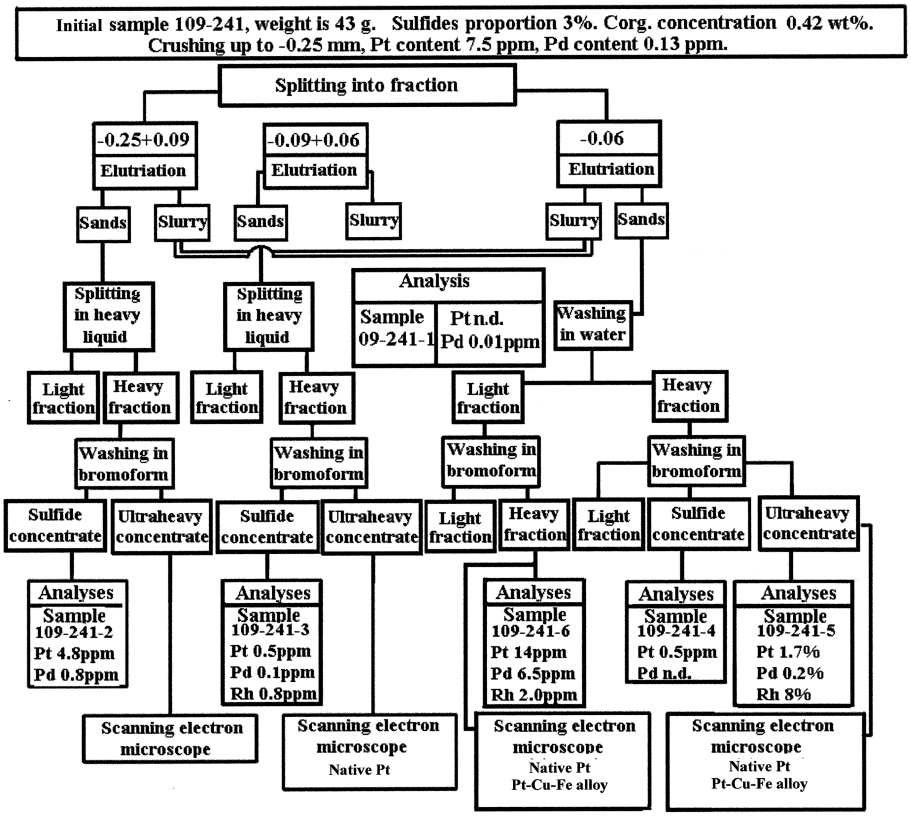

Fig. 10. Technological scheme for analyzing gold ore samples from the Sukhoi Log deposit.

Samples from the Sukhoi Log deposit were separated into fractions rich in carbon-bearing matter and sulfide concentrates in order to study the modes of PGE occurrences. Special techniques were used for PGE-enriched samples. We tried to detect the noble metals directly by electron microprobe analysis and X-ray photoelectron spectroscopy. The sulfide concentrates were studied with ore microscopy and mineral compositions were determined by electron microprobe. About 1000 mineral grains were analyzed by electron microprobe to determine the isomorphic PGE admixtures.

The scheme of the separation of ultraheavy concentrates is shown in Fig. 10. Sandy fractions of crushed rocks were divided into several size fractions (-0.25 to 0.09, -0.09 to 0.06, and -0.06 mm). Each size fraction was split in heavy liquids followed by cleaning of heavy fractions in bromoform to obtain light fractions, sulfide concentrates dominated by pyrite, pyrrhotite, and chalcopyrite, and ultraheavy concentrates with a varied mineralogy. Possible loss of PGE was controlled by chemical determination of PGE contents at selected stages. The output concentrates were analyzed for mineral compositions using a scanning electron microscope with EDS Link-10000. Ultraheavy concentrates were separated from samples previously determined to have contents of PGE of 1–7 ppm.

4. Mineralogy of platinum–gold zones

4.1. Main quartz–sulfide–gold mineralization

Ore minerals form only 3–5 vol.% of samples but include about 90 ore mineral species and varieties, including native metals, metal alloys, and sulfides (Table 1). In contrast to many other gold deposits, including black shale-hosted deposits, Fe–Ni–S and Ni–Co–Fe–As–S minerals are nearly as abundant as pyrite in the mineralized rocks of the Sukhoi Log deposit.

4.1.1. Native gold

Native gold, the main economic component of the deposit (Table 2), is commonly visible in polished sections, mainly as intergrowths with pyrite, pyrrhotite, pentlandite, galena, sphalerite, chalcopyrite, millerite, tetrahedrite, chlorite, tourmaline, quartz, and carbonates. The largest grains of native gold (50–150 μm) usually occur in relatively simple, one- or two-phase aggregates, whereas fine-grained gold (particles of about 10–20 μm) is common in multiphase aggregates. Particles of ultrafine-grained gold (a few microns in size) are included in pyrite, galena, and sphalerite. Gold of the Sukhoi Log deposit normally has a fineness as high as 893, but usually ranges from 850 to 900 (Table 3). Gold grains containing up to 24 wt.% of Ag are relatively rare and usually incorporate up to 1 wt.% of Cu and 1 wt.% of Hg.

4.1.2. Minerals of Fe–Ni–S system

Pyrite, the most abundant mineral of this system, usually occurs as coarse-grained porphyroblastic aggregates or as segregations in quartz–sulfide veinlets. Medium- and fine-grained aggregates are common as thin layers in gangue or wall rock matrix as are intergrowths of pyrite with pyrrhotite, chalcopyrite, cubanite, native gold, gersdorffite, and cobaltite. The chemical composition of pyrite is given in Table 4. Nickel contents up to 2.35 wt.% were found by electron microprobe analysis whereas detectable cobalt concentrations were found only in Ni-free pyrites. Early Ni-rich pyrites, containing more than 0.8 wt.% Ni, occur in the centers of large porphyroblasts. Most of the pyrite grains analyzed contain 0.0*n* to 0.*n* wt.% of As, but one grain contains 2.9 wt.% As. The As-free pyrites contain 0.02–0.2 wt.% of Sb. Sb- and As-bearing pyrites are known to be concentrators of "invisible" gold, which could constitute a significant proportion of the total gold content (Genkin et al., 1998).

Pyrrhotite is much less abundant than pyrite in ores, but occurs in grains as large as 0.5 mm in most samples. Two main pyrrhotite varieties are distinguished, one earlier than pyrite and the other coeval with or later than pyrite. The earlier pyrrhotite grains contain laminar, flame-shaped, and rounded or anhedral inclusions of pentlandite. Later intergrowths of pyrrhotite with native gold, chalcopyrite, galena, and sphalerite are common. The mineral composition (Table 4) ranges from Fe-rich hexagonal pyrrhotite to S-rich monoclinic pyrrhotite. Nickel contents in pyrrhotite vary from undetectable to 1.2 wt.%.

Table 1
Ore minerals of the Sukhoi Log deposit (Distler et al., 1996)

Class	Mineral	Formula	Class	Mineral	Formula
Native metals	Gold	Au	Arsenides and sulphoarsenides	Sperrylite	$PtAs_2$
	Platinum[a]	Pt		Niccolite	NiAs
	Silver	Ag		Maucherite	Ni_9As_{11}
	Iron[a]	Fe		Rammelsbergite	$NiAs_2$
	Tin[a]	Sn		Smaltite	$CoAs_{3-2}$
	Lead[a]	Pb		Safflorite	$CoAs_2$
	Copper[a]	Cu		Skutterudite	(Co, Ni)As_3
	Titanium[a]	Ti		Gersdorffite	NiAsS
	Tungsten[a]	W		Cobaltite	CoAsS
	Chromium[a]	Cr		Arsenopyrite	FeAsS
	Indium[a]	In		Enargite	Cu_3AsS_4
Metal solid solutions and intermetallic compounds	Gold–silver	(Au, Ag)	Tellurides and sulphotellurides	Altaite	PbTe
	Gold–silver–copper–mercury	(Au, Ag, Cu, Hg)		Calaverite[a]	$AuTe_2$
	Silver amalgam[a]	Hg_3Ag		Hessite[a]	Ag_2Te
	Platinum–Copper–Iron[a]	Pt_{1-2}(Cu, Fe)		Petzite[a]	Ag_3AuTe_2
	Platinum–Iron[a]	Pt_3Fe–PtFe		Cervelleite	Ag_4TeS
	Nickel–Tin[a]	(Ni, Sn)		Stutzite	Ag_7Te_4
	Nickel–Antimony[a]	(Ni, Sb)		Krennerite	Au_4AgTe_{10}
	Lead–Tin[a]	(Pb, Sn)		Joseite	BiTeS
	Antimony–Tin[a]	(Sb, Sn)	Selenides	Umangite	Cu_3Se
	Lead–Antimony–Tin[a]	(Pb, Sn, Sb)		Klockmannite	CuSe
	Copper–Zinc[a]	(Cu, Zn)		Berzelianite	Cu_2Se
	Tellur–Bismuth[a]	(Bi, Te)	Antimonides and salfosalts	Dyscrazite	Ag_3Sb
	Ag and Pb tellurobismuthide[a]	(Ag, Pb) (TeBi)		Galenobismuthite	$PbBi_2S_4$
	Pd and Ag tellurobismuthide[a]	(Pd, Ag) (TeBi)		Corynite	NiAsSbS
Sulfides	Pyrite	FeS_2		Tetrahedrite[a]	$Cu_{12}Sb_4S_{13}$
	Cooperite	PtS		Cylindrite[a]	$Pb_3Sn_4Sb_2S_4$
	Pyrrhotite	$Fe_{1-x}S$	Oxides, phosphates and tungstates	Rutile	TiO_2
	Pentlandite	$(Fe, Ni)_9S_8$		Baddeleyite	ZrO_2
	Cubanite	$CuFe_2S_3$		Magnetite	Fe_3O_4
	Chalcopyrite	$CuFeS_2$		Scheelite	$CaWO_4$
	Millerite	NiS		Wolframite	(Fe, Mn)WO_4
	Mineral $NiFe_2S_4$[a]	$NiFe_2S_4$		Monazite[a]	(La, Ce, Nd)PO_4
	Mineral Ni_3FeS_4[a]	Ni_3FeS_4		Xenotime[a]	YPO_4
	Heazlewoodite	Ni_3S_2	Halides	Iodyrite[a]	AgJ
	Violarite	$FeNi_2S_4$		Mineral (Pb, Bi)Cl_2[a]	(Pb, Bi)Cl_2
	Sphalerite	ZnS		Mineral $PtTlCl_4$[a]	
	Galena	PbS			
	Molybdenite	MoS_2			
	Greenockite[a]	CdS			
	Acanthite	Ag_2S			
	Bisulfide of Re[a]	ReS_2			

[a] Minerals distinguished by authors.

Pentlandite usually occurs as small inclusions in pyrrhotite but also as separate grains coexisting with millerite and heazlewoodite. Electron microprobe analysis shows compositions ranging from 13.7 to 36.3 wt.% Fe and 30.0 to 48.3 wt.% Ni. The ΣMe/S are close to the stoichiometric ratio. Small As and Sb contents occur in some pentlandite grains, but no Co or Cu were detected.

Millerite with up to 3.5 wt.% Fe forms intergrowths with pyrite and other minerals, including native gold. Up to 0.16 wt.% of As, Sb, and Cu occur in some millerite. Violarite is close to pentlandite in

Table 2
Concentration of ore elements in bulk-rock samples from drill core 6 by INAA analysis (ppm)

H, m	Au	Ag	As	H,m	Au	Ag	As
171	0.08		33.44	216	2.28	2.87	27.40
172	0.07	2.94	24.59	217	3.03		54.22
173	2.87		103.8	218	0.27	4.08	47.37
174	0.03		35.83	219	11.14	3.67	59.61
175	0.01		8.06	220	1.76	4.01	49.06
176	0.16		30.21	221	5.51	2.41	112.8
177	0.55	3.00	23.37	222	3.32	3.87	51.58
178	6.06	2.57	23.60	223	0.50	2.84	52.31
180	0.33		23.94	224	1.11	2.83	50.03
181	0.09	3.21	23.03	225	8.93	2.73	69.82
182	0.13	2.89	21.87	226	2.78		66.73
183	1.32		41.92	227	0.37		
188	0.11	4.79	20.61	228	32.82	9.34	31.25
189	1.58	3.44	29.77	229	7.32		74.91
190	1.52		37.07	230	0.68		20.46
191	0.25	2.98	16.95	231	10.36	3.73	17.10
192	12.06	3.24	51.16	232	0.37	2.77	15.22
193	1.65	3.00	51.76	233	0.14	4.55	35.87
194	0.75	2.17	31.75	234	4.48	2.92	22.21
195	4.51	2.52	35.35	234	0.55	2.53	20.56
196	1.29		54.54	235	0.44	3.21	32.31
197	1.78	2.64	73.53	235	0.36		43.83
198	11.00	3.04	36.49	236	0.08	2.38	22.66
199	0.65	2.41	15.11	237	1.01	0.48	5.63
200	1.69		32.44	238	0.01	0.38	1.64
201	22.82		43.43	239	0.07	3.10	52.25
202	0.92	2.72	49.69	240	0.15	3.56	34.90
203	0.90	4.40	41.75	241	0.12	3.06	27.96
204	0.21		43.28	242	0.26		34.84
205	2.53	5.32	37.38	243	0.47		33.44
206	0.64		71.69	244	7.28	3.84	45.34
207	1.42		53.94	245	2.53		18.77
208	2.27		59.14	246	0.17	4.27	
209	1.55		49.99	247	12.94	2.68	43.61
210	2.31	3.77	63.21	248	0.47		53.69
211	6.82	5.04	77.90	249	1.46	2.50	29.92
212	11.88	3.57	73.19	250	2.05	4.78	26.12
213	5.14	3.85	48.78	251	0.55		38.09
214	8.60	3.24	51.24	252	0.11		
215	3.25	3.26	68.79	254	0.11	2.18	32.73

H—depth in meters; blank—not detected.

chemical composition, differing by its higher sulfur content. It is found as fine idiomorphic and anhedral grains but may be pseudomorphous after earlier pentlandite. Electron microprobe analysis reveals single tiny (10–30 μm) grains of two other Fe–Ni–S minerals, a Fe-rich violarite-like mineral with a composition of $NiFe_2S_4$ and a millerite-like mineral with a composition of Ni_3FeS_4.

4.1.3. Minerals of Ni–Co–Fe–As–S system

Co, Ni, and Fe sulfarsenides are represented as nearly pure arsenopyrite and gersdorffite and phases of variable composition from Fe-rich gersdorffite up to Fe–Ni-rich cobaltite (Table 4) (Fig. 11). Arsenopyrite is the least abundant of the sulfarsenides, occurring as fine idiomorphic crystals usually in pyrrhotite and free of Ni and Co.

Table 3
Representative electron microprobe analyses of native gold (wt.%)

N	Au	Ag	Cu	Σ	N	Au	Ag	Cu	Σ
1	75.57	24.51		100.08	42	89.34	9.07	0.05	98.46
2	78.35	18.55		96.9	43	89.5	9.7		99.2
3	81.31	17.83		99.14	44	89.6	10.1		99.7
4	83.49	16.05		99.54	45	89.71	9.24	0.03	98.98
5	84.02	16.58	0.06	100.66	46	89.75	9.61	0.03	99.39
6	85.3	15.07	0.09	100.46	47	90.1	9		99.1
7	85.85	15.06	0.08	100.99	48	90.1	9.1		99.2
8	86.05	10.31		96.36	49	90.3	9.2		99.5
9	86.2	13.3		99.5	50	90.3	9		99.3
10	86.38	12.17		98.55	51	90.42	10.53	0.02	100.97
11	86.7	12.6		99.3	52	90.5	9.3		99.8
12	86.9	12.5		99.4	53	90.54	9.91	0.03	100.48
13	86.92	10.59		97.53	54	90.6	8.7		99.3
14	87.02	11.74		98.76	55	90.7	9.1		99.8
15	87.15	9.6	0.07	96.82	56	90.9	8.4		99.3
16	87.2	12		99.2	57	91.24	10	0.04	101.28
17	87.25	10.88	0.11	98.24	58	91.27	8.36	0.05	99.68
18	87.29	9.23	0.03	96.55	59	91.3	8.6		99.9
19	87.38	14.16	0.01	101.54	60	91.4	8.3		99.7
20	87.42	12.85	0.05	100.42	61	91.4	8.1		99.5
21	87.59	9.68	0.01	97.28	62	91.6	8.2		99.8
22	87.6	12		99.6	63	91.6	8.3		99.9
23	87.6	12.1		99.7	64	91.8	7.6		99.4
24	87.6	12		99.6	65	92	7.8		99.8
25	87.69	9.76	0.03	97.48	66	92.06	10.18	0.03	102.27
26	88.08	11.34	0.05	99.47	67	92.1	7.3		99.4
27	88.14	9.71	0.03	97.89	68	92.2	7.8		100
28	88.23	10.36		98.59	69	92.4	7.2		99.6
29	88.3	11.36	0.02	99.68	70	92.8	6.6		99.4
30	88.38	9.59	0.01	97.98	71	92.9	6.5		99.4
31	88.4	11.34	0.02	99.76	72	92.9	6.1		99
32	88.6	10.9		99.5	73	93.3	6.2		99.5
33	88.6	10.8		99.4	74	93.4	6.3		99.7
34	88.6	11.3		99.9	75	93.8	6		99.8
35	88.6	11.2		99.8	76	93.8	5.9		99.7
36	89	10.7		99.7	77	94.1	5.7		99.8
37	89.2	10.6		99.8	78	99.2	0.5		99.7
38	89.21	12.8		102.01	79	99.4			99.4
39	89.21	9.55	0.02	98.78	80	99.5	0.1		99.6
40	89.21	10.92		100.13	81	99.6	0.3		99.9
41	89.3	9.27	0.03	98.6	82	99.7			99.7

Blank—below detection limits.

Table 4
Representative chemical composition of Fe–Ni–S and Ni–Co–Fe–As–S minerals of the Sukhoi Log deposit by electron microprobe analysis (wt.%)

n	Минерал	Ni	Fe	S	As	Co	Sb	Cu	Σ
1	Py		44.33	53.72	0.56	1.19			99.82
2	Py	0.03	46.4	53.86	0.25	0.16		0.01	100.71
3	Py	0.38	47.46	51.3					99.14
4	Py	0.84	46.76	53.68				0.01	101.29
5	Py	1.04	46.47	52.86	0.05	0.03		0.04	100.49
6	Py	1.63	45.91	52.75	0.07		0.14		100.5
7	Py	2.25	43.75	54.55	0.05			0.07	100.67
8	Po		62.3	37.9					100.2
9	Po	0.12	60.69	39.88		0.07		0.01	100.77
10	Po	0.32	60.85	39.24		0.01		0	100.42
11	Po	0.59	60.76	38.34				0.01	99.7
12	Po	1.2	57.86	40.74	0.01	0.03			99.84
13	Pn	30	36.3	33.5					99.8
14	Pn	35.06	31.52	33.4	0.05			0.05	100.08
15	Pn	39.85	26.26	33.25					99.36
16	Pn	40.95	23.5	35.64		0.01			100.11
17	Pn	42.92	24.35	31.96	0.08		0.01		99.32
18	Pn	44.79	21.09	33.97	0.01				99.86
19	Pn	47.93	14.68	36.1		0.01			98.72
20	Mil	55.87	6.24	36.89					99
21	Mil	59.89	2.92	36.31				0.08	99.2
22	Mil	60.52	4.36	36.4	0.08			0.11	101.47
23	Mil	62.36	2.48	34.23	0.06		0.02		99.15
24	Mil	63.07	2.72	34.19	0.36	0.03		0.09	100.46
25	Mil	63.52	1.37	35.87	0.23		0.04	0.02	101.05
26	Mil	63.81	2.16	34.2	0.06		0.02	0	100.25
27	Mil	64.14	1.76	33.69	0.08		0.02		99.69
28	Mil	64.27	1.92	33.23					99.42
29	Mil	64.95	0.62	35.36	0.05	0.02		0.06	101.06
30	Mil	65.94	0.51	34.15	0.08	0.06			100.74
31	Ars		34.5	19.6	45.2				99.3
32	Ars		34.2	19.4	45.7				99.3
33	Cb	1.79	6.86	24.09	39.74	28.66		0.05	101.19
34	Cb	2.8	6.5	20.1	44.5	25.3			99.2
35	Cb	3.9	7.2	20	43.8	25.1			100
36	Cb	6.1	7.9	20.2	43.4	21.7			99.3
37	Cb	10.6	8.6	18.7	44.4	16.9			99.2
38	Cb	11.3	11.5	18.8	44.8	12.9			99.3
39	Gf	16.65	12.78	19.59	43.68	6.33	0.01	0.01	99.05
40	Gf	17.74	12.12	19.26	43.87	6.84			99.83
41	Gf	20.03	12.98	19.95	44.72	2.11	0.01	0.02	99.82
42	Gf	21.28	13.93	20.01	44	1.04	0.01		100.27
43	Gf	32.39	1.28	18.82	44.24	1.12	0.31	0.01	98.17
44	Gf	32.46	1.45	18.65	44.03	1.16	0.29	0.02	98.06
45	Gf	33.88	0.81	20.07	43.69	0.83	0.46		99.74
46	Gf	34.68	2.87	19.45	43.24	0.28	0.16	0.15	100.83
47	Viol	30.92	23.3	42.26				0.32	96.8
48	Viol	31.38	24.78	44.94			0.02	0.05	101.17
49	Viol	32.87	23.54	43.32	0.05		0.04		99.82
50	Viol	34.54	21.72	42.2	0.01	0.17	0.02	0.28	98.94
51	Viol	36.3	21.03	43.19					100.52
52	Viol	40.16	16.97	43.34	0.03		0.03		100.53

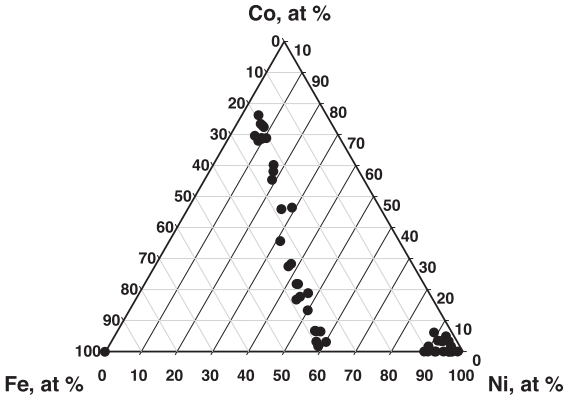

Fig. 11. Composition of Fe–Ni–Co–As–S minerals (cobaltite–gersdorffite, arsenopyrite) in ores of the Sukhoi Log deposit.

Gersdorffite commonly occurs as anhedral inclusions in pyrite or as individual euhedral grains and aggregates in gangue minerals. Arsenopyrite, sphalerite, and native gold are found intergrown with gersdorffite, which contains ≤1 at.% of Fe and Co. Iron-poor (0.76–3.65 wt.% of Fe) and iron-rich (11.8–13.83 wt.% of Fe) compositional varieties of gersdorffite are distinguished. Elevated Co contents are typical of iron-rich gersdorffite.

Fe-rich gersdorffite and Fe–Ni-rich cobaltite are observed as inclusions in pyrite and in intergrowths with pyrrhotite and pentlandite and form an isomorphous series, in which Ni and Co content varies and Fe contents are fairly stable (20–40 àt.% Fe). The end-member varieties of this series contain 1.8 wt.% Ni, 28.7 wt.% Co, 24 wt.% Ni, and less than 1 wt.% Co (Fig. 11).

4.1.4. Minor and rare minerals

Minor ore constituents include galena, tetrahedrite and sphalerite and other rare minerals (Table 1) some of which were reported by Vikulova et al. (1977). They generally occur as inclusions of about 1 μm in size in pyrite crystals associated with native gold.

Galena occurs as intergrowths with chalcopyrite, pyrite, native gold and native silver and it can contain up to 0.55 wt.% Ag, up to 1.36 wt.% Bi, up to 0.17 wt.% Te. Tetrahedrite occurs as intergrowths with chalcopyrite, galena, pyrite, millerite, and native gold. It contains 36.0 wt.% Cu, 1.2 wt.% Fe, 7.8 wt.% Zn, 27.6 wt.% Sb, 1.3 wt.% As, and 26.2 wt.% S.

Sphalerite is associated with pyrite, pyrrhotite, galena, and native gold and forms two main varieties: one with iron content lower than 0.8 wt.% and the other with iron contents ranging from 4.2 to 5.1 wt.%. Considering that the iron content in sphalerite depends on temperature and sulfur activity (Barton and Toulmin, 1966), it seems likely that the Fe-poor sphalerite variety crystallized at aS_2 corresponding to the pyrite buffer, whereas the Fe-rich sphalerite formed under the conditions of pyrite–pyrrhotite buffer. The cadmium concentrations in sphalerites are uniform (0.2–0.4 wt.%) regardless of the iron contents. Greenockite (CdS) was found in ultraheavy concentrate that is enriched in PGE contents and contains 73.0 wt.% Cd, 2.6 wt.% Zn, and 23.4 wt.% S.

4.1.5. Oxides, carbonates, phosphates, and tungstates

Multistage hydrothermal–metasomatic carbonatization occurred during of the main ore-forming process. Hydrothermal carbonates are observed in the quartz–sulfide veinlets and in thick quartz veins. The evolution of carbonate composition is given in Table 5 and Fig. 12. Fine-grained matrix carbonates are mainly ankeritic in composition. Larger porphyroblasts and carbonates from the quartz–sulfide veinlets are mainly magnesian siderite; ankerite is less often found as porphyroblasts. Some porphyroblasts are characterized by compositional zoning, oscillating between 1 and 3 wt.% MgO. Siderite compositions from in the quartz–sulfide veinlets range from as much as 45 wt.% Fe and about 11 wt.% Mg in other cases.

Monazite and magnetite are common in the ore, whereas scheelite, wolframite, baddeleyite, and xenotime are rare. Monazite-I forms rounded por-

Note to Table 4:
Py—pyrite, Po—pyrrhotite, Pn—pentlandite, Mil—millerite, Viol—violarite, Ars—arsenopyrite, Cb—cobaltite, Gf—gersdorffite; blank—not detected.

Table 5
Composition of Fe–Mg carbonates of the Sukhoi Log deposit by microprobe analysis (wt.%)

Sample	Mineral	FeO	MnO	CaO	MgO	CO_2
Fine-grained matrix carbonates						
109235	Ankerite	11.14	2.93	25.94	12.24	47.75
109235	Ankerite	11.59	0.75	25.82	13.5	48.34
112204	Ankerite	11.91	0.56	26.99	13.7	46.84
112084	Ankerite	12.36	1.43	26.15	13.3	46.76
Porphyroblasts and recrystallized carbonates						
112204	Mg-siderite, centre	35.83	0.58	0.41	20.83	42.35
112204	Mg-siderite, rim	38.41	1.68	0.32	16.65	42.94
112184	Mg-siderite, centre	37.37	1.25	0.38	20.03	40.97
112184	Mg-siderite, rim	36.57	1.61	0.29	17.23	44.3
112184	Mg-siderite, centre	37.4	1.29	0.34	20.03	40.94
112184	Mg-siderite, centre	37.37	1.37	0.32	20.18	40.76
112184	Mg-siderite, rim	35.62	0.59	0.41	21.69	41.69
36090	Mg-siderite	29.91	0.17	0.31	21.57	48.04
112038		32.29	0.14	0.35	20.81	46.41
112104		33.35	0.93	0.34	18.74	46.64
36090		35.62	0.61	0.31	18.35	45.11
112038		36.43	0.96	0.25	18.07	44.29
112084		37.1	0.76	0.35	20.21	41.58
112038		38.21	0.99	0.36	13.74	46.7
112104	Ankerite	10.61	2.76	24.77	11.16	50.7
112164	Ankerite	10.65	0.32	26.29	14.36	48.38
Carbonates in quartz–sulfide veinlets						
112062	Mg-siderite	33	1.1	0.55	21.04	44.31
112062		38.94	0.89	0.25	15.22	44.7
51109		40.37	1.08	0.14	15.34	43.07
112027		43.22	0.7	0.35	11.67	44.06
51109		44.86	0.63	0.95	10.54	43.02

CO_2 content = 100% − sum of oxides.

phyroblasts up to 0.5 mm in diameter (Fig. 13a) and is most abundant in sericite layers with carbonaceous matter. Monazite is also found as extended lenses or veinlets in the quartz–sericite matrix (Fig. 13b). Monazite-I apparently represents an authigenic mineral of the black shale transformed by metamorphism. Monazite-II is observed as aggregates or as skeletal crystals up to 200 μm in pyrite in association with microinclusions of native gold, pyrrhotite, galena (Fig. 13c,d), quartz, pyrite, and albite. Monazite is characterized by a heterogeneous internal constitution with variable concentrations of REE and Th in phases. Hydrothermal metamorphogenic monazites differ in Nd, Ce, and La contents. All monazites are Ce-rich, but in some cases Nd becomes dominant (Table 6). Th concentrations are as high as 6.7 wt.%. Hydrothermal and authigenic monazites form a continuous compositional series, but hydrothermal grains are more uniform in REE composition with a wider range of Th contents.

4.1.6. Native metals, metal solid solutions, and intermetallic compounds

The deposit contains many native metals besides native gold and silver (Table 1). Native platinum, iron, chromium, tungsten, titanium, lead, tin, and copper occur in ultraheavy concentrates, commonly intergrown with other ore minerals. The native metals occur as anhedral grains a few microns to a few tens of microns in size, which are similar in habit to PGE minerals. Native chromium is located in interstices in the rock-forming silicates, where a Cl-rich phase also occurs, but also with native tungsten, Pt–Fe solid solutions, and native gold.

Intergrowths of native metals include native tin and lead, which form aggregates where tin droplets are included in a lead matrix, or vice versa. Ni–Sn metallic solid solutions were also found in intergrowths with these aggregates, which may result from exsolution.

Silver is found in native form as well as in sulfide, sulfosalts, tellurides, and halides. Native

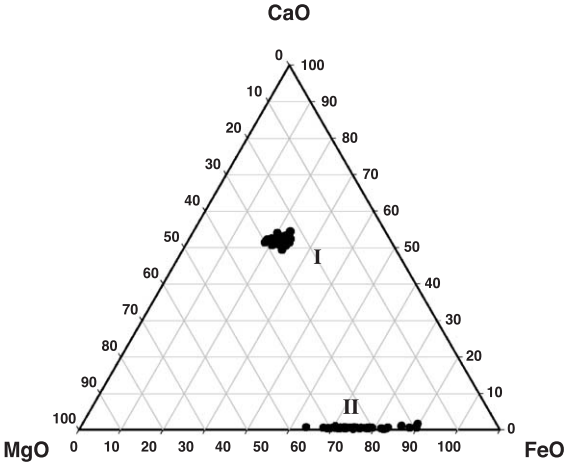

Fig. 12. Chemical composition of carbonates from sedimentary matrix (I), metamorphogenic porphyroblasts and quartz–sulfide veinlets (II).

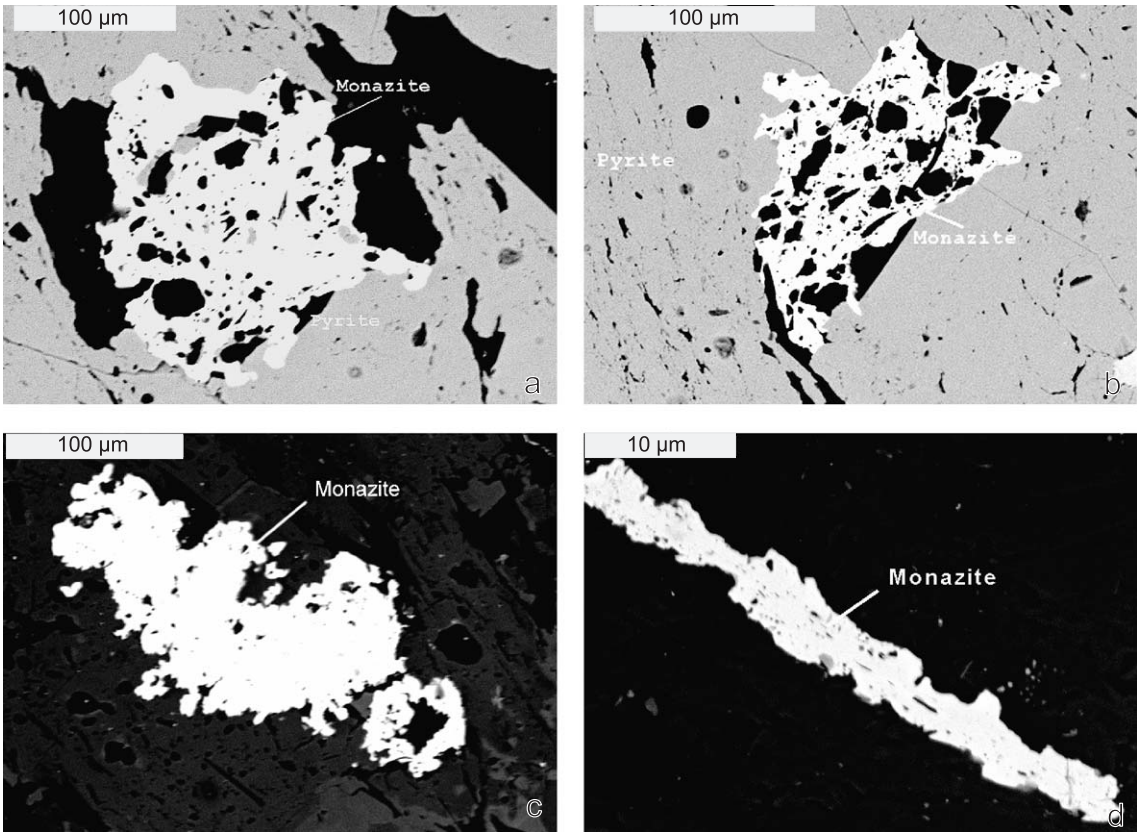

Fig. 13. Monazite grains. (a) Porphyroblast in black shale; (b) lenticular grain in black shale; (c, d) inclusions in pyrite.

tellurium is incorporated in a Te–Bi solid solution, found as tiny equant particles about 3 μm in size together with a Ni–Sb phase as inclusions in native gold. Tin occurs in binary and ternary alloys of variable composition with Ni, Sb, and Pb as well as in sulfosalts such as cylindrite. Iron is present in

Table 6
Chemical composition of monazite by EDS Link-10000 (wt.%)

Sample	Si	P	Ca	Mn	Fe	La	Ce	Pr	Nd	Sm	Eu	Gd	Tb	Dy	Ho	Er	Tm	Yb	Th
36101	0.70	11.99				2.85	16.85	4.76	22.88	7.38		2.54						1.21	
36101	0.46	12.63				3.47	17.71	3.69	23.53	5.91		2.76							
36161	0.82	10.38		0.88		4.82	20.08	4.49	19.84	5.84		3.28							
112086		11.27			1.42	5.06	20.81	3.99	19.66	4.43	1.73	2.88		0.72					1.44
36101	0.59	11.03				9.35	21.77	3.48	15.96	3.82		1.93							2.86
36161	0.76	10.83	0.76			10.97	21.10	2.61	12.49	3.90		2.86							5.83
36161	0.72	10.75				11.09	24.24	3.54	14.85	3.79		1.49	1.06						2.34
112141	0.38	11				12.27	31.05	2.74	12.55	1.11		0.98							2.43
112141	0.75	9.8				13.67	24.95	2.93	13.05	2.84	1.68	0.93				1.07			3.71
112086		12.29			1.96	14.55	28.77	1.85	9.54										
36161	0.33	11.16				14.68	30.28	4.28	8.68	1.86									
36101	0.51	11.77				18.85	28.75	3.04	6.52										
36101	0.82	12.16				21.98	31.38	2.51	5.74					1.01					

Blank—not detected.

the native form; it is also incorporated in metallic solid solutions with Cr, Ti, and W, as well as in numerous sulfides, sulfosalts, and sulfarsenides and other minerals. Copper occurs as Cu–Zn alloys, various sulfides and sulfosalts of Cu and Zn. Lead enters a Pb–Sn alloy and forms intermetallic compounds with Ag, Bi, Te, sulfides, and sulfosalts. Tungsten is incorporated in a W–Ti–Fe solid solution, scheelite, and wolframite.

Many native metals form intergrowths with each other or form aggregates with exsolution textures and are probably coeval. Grains of native metals and metallic alloys are also found as inclusions in minerals of gold-bearing assemblages. For example, Ni–Sb, Ni–Sn, and Te–Bi inclusions occur in native gold.

Textural relations of ore minerals, observed in the polished sections, demonstrate that native elements and S-poor sulfides formed during the early stages of mineralization. Increasing activity of sulfur results in sulfosalts and S-rich sulfide deposition.

The metallic phases of ore-forming elements, including PGE, coexist within the stability fields of iron- and S-poor pyrrhotite–nickel, nickel–Fe-rich pyrrhotite–Fe-rich pentlandite, and, possibly, Ni-rich pentlandite–heazlewoodite, whereas the main gold-bearing assemblages are confined to fields richer in sulfur (Fig. 14).

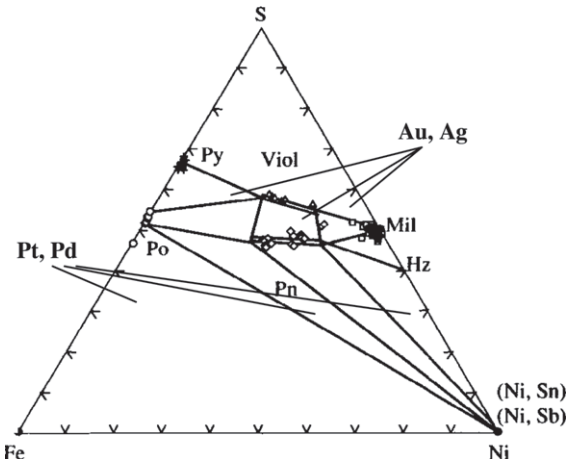

Fig. 14. Composition (at %) of Fe–Ni–S minerals in ores at the Sukhoi Log. Py—pyrite; Viol—violarite; Po—pyrrhotite; Pn—pentlandite; Mil—millerite; Hz—heazlewoodite; (Fe, W, Cr), (Ni, Sn), (Ni, Sb)—metal solid solutions; native Pt, Pd and Au, Ag.

Table 7
Concentration of Pt, Pd, Au, and Ag (ppm) in bulk samples, sulfide and ultra-heavy concentrates

N	Sample	Pt	Pd	Au	Ag
Supraore zone	36 101	0.18	0.02		4.51
	36 109	0.12	0.04	0.017	1.55
	36 125	1.6	0.02		1
	36 161	0.05	0.03	0.62	3.52
	112 027	0.75	0.005	7.8	n.d.
	112 043	0.39	0.005	0.014	n.d.
	112 052	0.28		1.3	n.d.
	112 062	0.3		1.2	n.d.
	112 067	0.39	0.006	2	n.d.
	112 078	0.27	0.002	5.6	n.d.
	112 085	0.14	0.002	26	n.d.
	203 083	0.31	0.05	0.31	0.86
Ore zone	203 098	0.07	0.07	7	12.34
	203 109	0.06	0.13	0.06	1.08
	203 119	0.06	0.018	0.25	2.26
	203 128	0.12	0.016	0.34	0.69
	203 140	0.12	0.034	1.2	0.7
	203 149	0.02	0.016	2.8	1.3
	203 162	0.23	0.007	0.12	5.65
	203 173	0.4	0.009	0.29	0.75
	36 189	0.55	0.03	8.5	6.53
	36 200	0.2	0.005	4.8	2.33
	36 221	0.05	0.01	0.26	2.49
	10–120[a]	0.5	0.003	1.00	n.d.
	10–121[a]	0.67	0.005	15.2	n.d.
	10–167[a]	1.36	0.045	0.4	n.d.
	2–219[a]	0.026	0.43	n.d.	n.d.
Infraore zone	109 185	0.11	0.02	0.41	n.d.
	109 191	0.09	0.003	0.086	n.d.
	109 198	0.08	0.015	0.2	n.d.
	109 208	0.07	0.003	0.035	n.d.
	109 219	0.06	0.009	0.011	n.d.
	109 239	0.07	0.008	0.015	n.d.
	109 241	7.5	0.03	0.042	n.d.
	36 244	0.04	0.02	0.22	1.88
	36 274	0.02	0.06		0.55
Sulfide	6103[a]	0.26	0.35	0.31	1.8
concentrates	6104[a]	8.30	0.33	0.83	11.0
	6120.3[a]	0.02	0.13	21.00	6.8
	6130.7[a]	0.16	0.37	0.57	3.9
	6153[a]	0.01	0.26	1.40	10.0
	6165[a]	0.06	0.52	1.30	24.0
	6173[a]	0.02	0.14	1.20	10.0
	6197.3[a]	1.50	0.26	91.00	19.0
	6221[a]	0.26	0.22	13.00	19.0
	6240[a]	0.00	0.71	0.55	1.8
	6242[a]	0.00	0.42	3.30	11.0
UHC	109 241	17 000	2000	n.d.	n.d.

Data of chemical analysis; n.d.—not determined; blank—not detected; UHC—ultra-heavy concentrate.
[a] Data of ICP-MS.

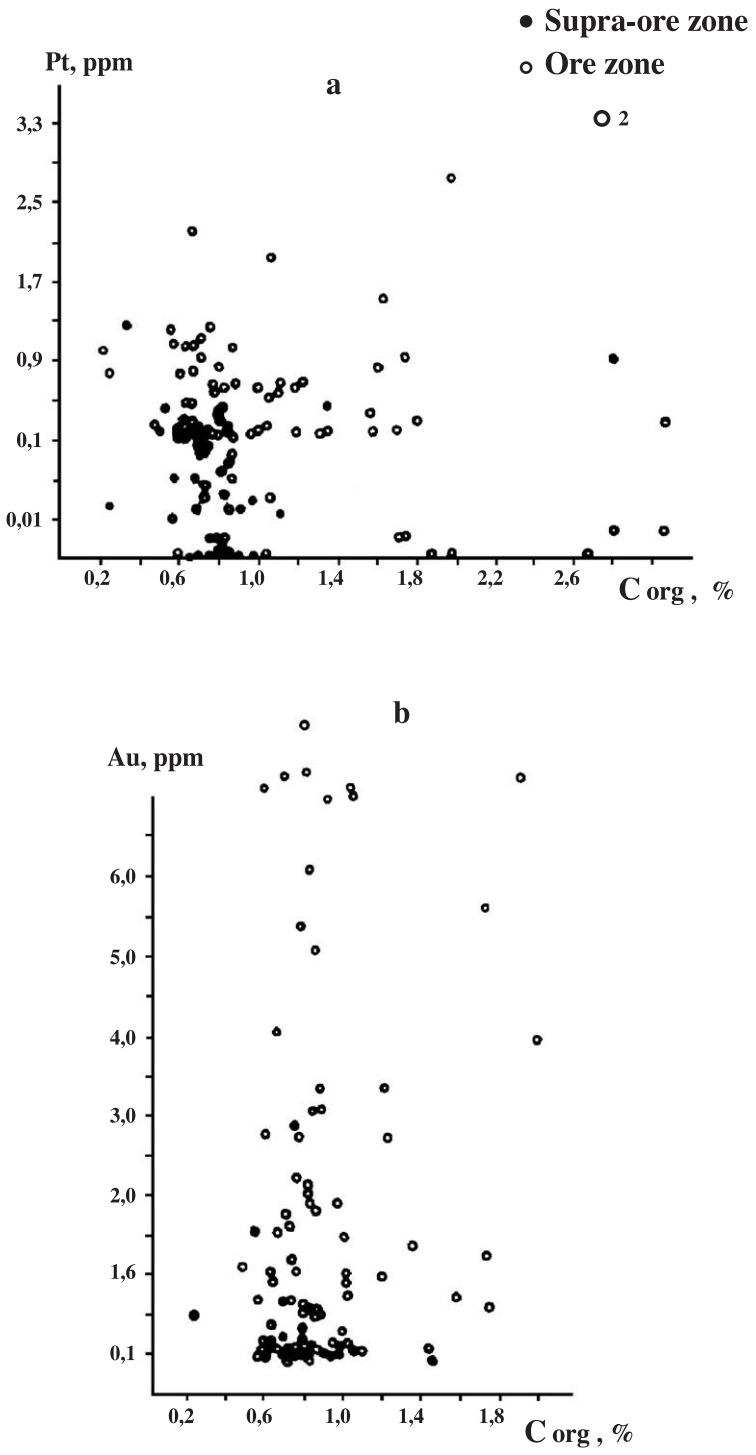

Fig. 15. Correlation of organic carbon contents with Pt (a) and Au (b) concentrations. Supra-ore zone and ore zone.

4.2. PGE mineralization

4.2.1. General features

Native platinum is the most abundant PGE mineral at the Sukhoi Log deposit (Table 7) as determined from analyses of more than 400 samples from different vertical sections of the gold-bearing zone as well as the overlying and underlying rocks.

Platinum contents higher than 0.1 ppm are limited to the hydrothermal–metasomatic halo and the zone of sulfide mineralization. Such concentrations were determined in all rocks of supra-ore, protore, and infra-ore zones. Platinum concentrations higher than 1 ppm occur in the part of the supra-ore zone adjacent to the mineralized zone as well as within the protore itself, with the highest concentrations (up to 3–5 ppm) found in the upper part of the gold protore. Elevated platinum concentrations are irregularly distributed in the infra-ore zone.

Thus, the platinum concentrations mainly lie outside of the zone of highest gold contents as reflected in the absence of correlation between Pt and Au values. No significant correlation exists between Pt and organic carbon content or between Au and organic carbon content (Fig. 15).

Other PGE show a similar distribution pattern. The concentrations of palladium, however, are one order of magnitude lower than that of platinum, whereas the other PGE were detected only in some cases. For example, the highest contents of Rh (up to 0.8 ppm) correspond to the highest platinum concentrations.

4.2.2. PGE mineralogy

Chemical analyses of ore concentrates and electron microprobe analyses of individual phases show that the proportion of PGE incorporated as solid solution in sulfides is not significant in the Sukhoi Log deposit as shown by microprobe analysis of more than 1000 grains of pyrite, pyrrhotite, pentlandite, chalcopyrite, millerite, and minerals of the cobaltite–gersdorffite series. The PGE contents were mostly found to be lower than the detection limit of 0.01 wt.% but Pd contents up to 0.12 wt.% were established in separate grains of cobaltite. Relatively high PGE contents were found by microprobe in some grains of pyrite, pentlandite, other nickel sulfides, arsenides, and sulfarsenides but may result from tiny inclusions of PGE minerals, such as the microscopic cooperite inclusion in pyrite reported by Mitrofanov et al. (1994).

The highest PGE contents occur in the finest and densest fraction of the separates. One sample from an ultraheavy (PGE) concentrate (size fraction −0.06 mm) contains 9.9 wt.% of total PGE. The weights of fractions (Fig. 10) were: 2—0.127 mg, 3—0.024 mg, 4—19.5 mg, 5—0.5 mg, 6—0.0076 mg. Scanning electron microscopy showed that ultraheavy fractions generally contain PGE minerals as separate grains and more rarely as intergrowths with ore-forming sulfides. Native platinum, Pt–Fe–Cu alloys, Pt–Fe alloys, sperrylite, and cooperite were found in the ultraheavy concentrates.

Native platinum occurs as individual grains up to 10 μm (Fig. 16e,f) and in intergrowths with pyrite, which commonly have anhedral or dendritic shapes (Fig. 16a–c). Pt–Fe–Cu alloys dominate the PGE mineral grains analyzed (Table 8). They occur as separate grains about 5–10 μm in size and as inclusions and intergrowths with pyrite, cobaltite, carbonate, and quartz (Fig. 16d). Varieties with atomic ratio Pt:(Cu+Fe) from 1.4:1.6 to 2:1 were distinguished. A phase with composition close to Pt(Cu,Fe) was found and a phase with (Cu+Fe)>Pt corresponding to $Pt_{0.85}(Cu,Fe)_{1.0}$ was analyzed. Thus, a series of disordered (and possibly continuous) solid solutions $Pt_2(Cu,Fe)_1$–Pt(CuFe) with dominant Cu occur in the mineralized zone. The Fe-rich variety may be transitional to the Pt–Fe series. Pt–Fe solid solutions have the same morphological features as Pt–Fe–Cu alloys and occur in the same mineral associations. There is no evidence for extensive miscibility between (Pt,Cu) and (Pt,Fe) for which significant Cu peaks are

Fig. 16. Platinum minerals in ores of the Sukhoi Log deposit. Scanning electron microscope. All bar scales in micrometers (μm). (a) A skeletal crystal of native platinum; (b) intergrowth of native platinum with pyrite; (c) grain of native platinum in pyrite; (d) intergrowth of native platinum with Fe–Mg carbonate (Carb) in cobaltite (Cob); (e) inclusions of native platinum in sericite (Ser); (f) inclusion of native platinum in Fe–Mg carbonate (Carb); (g) crystals of sperrylite ($PtAs_2$); (h) crystal of cooperite (PtS) with pyrite.

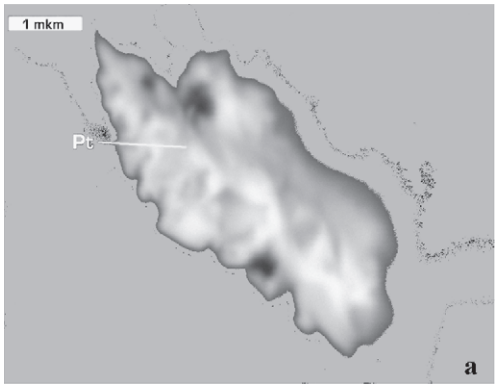
1 mkm
Pt
a

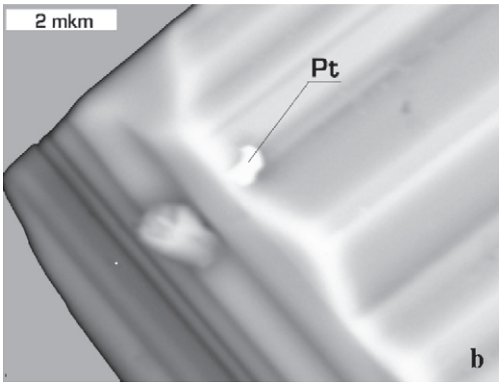
2 mkm
Pt
b

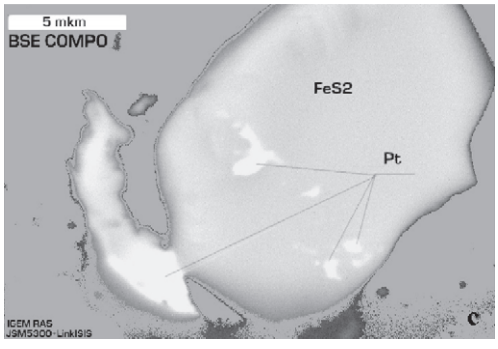
5 mkm
BSE COMPO
FeS2
Pt
ICEM RAS
JSM5300 LinkISIS
c

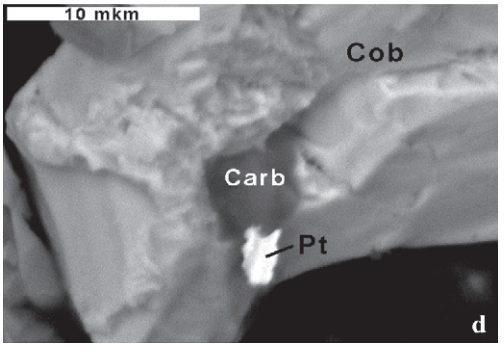
10 mkm
Cob
Carb
Pt
d

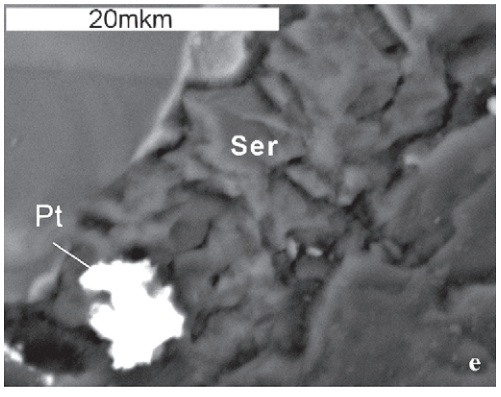
20mkm
Ser
Pt
e

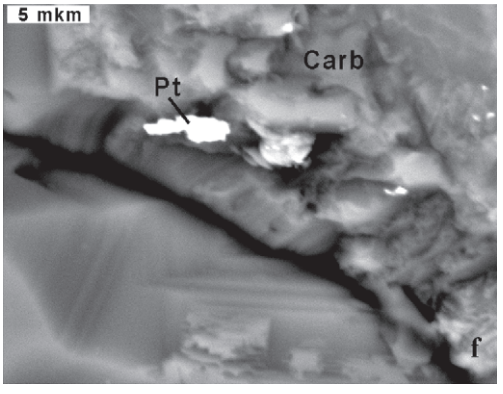
5 mkm
Carb
Pt
f

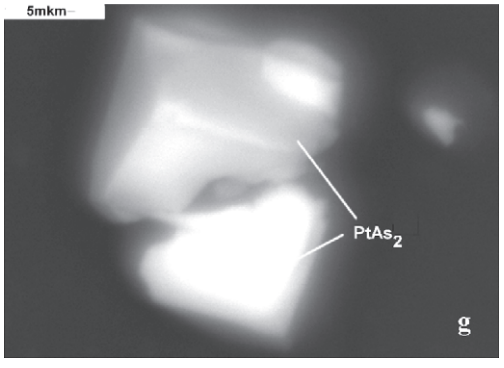
5mkm
PtAs2
g

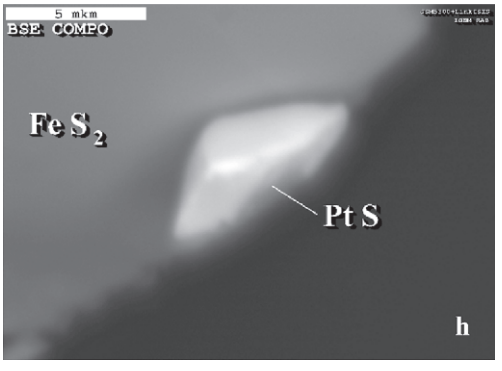
5 mkm
BSE COMPO
Fe S2
Pt S
h

Table 8
Chemical composition (wt.%) of platinum minerals from the Sukhoi Log deposit by EDS Link-10000

Mineral	Pt	Cu	Fe	Ag	Au	As	S	Σ
Native platinum	97.44	1.12						98.56
Pt–Cu–Fe alloy	84.12	11.31	4.35					99.78
	82.55	12.84	4.7					100.09
	80.65	16.21	2.5					99.36
	79.13	14.96	2.60					96.69
	77.76	21.06	1.90					100.72
	77.13	18.38						95.51
	71.54	26.20	0.8					98.54
Pt–Fe alloy	73.65		15.60					99.25
	89.27		8.82					98.09
Sperrylite	52.91	1.27	0.19			45.26		99.63
	55.44	0.82		0.33	0.93	42.15		99.67
	53.32			0.05	1.11	44.79		99.27
Cooperite	86.4						13.7	100.1

Blank—not detected.

usually absent. The atomic ratios Fe/Pt show that most of the analyzed grains consist of Pt_3Fe or PtFe.

Sperrylite is confined to the supra-ore zone associated with low-grade quartz–sulfide veinlets and occurs as idiomorphic crystals about 10 μm in size (Fig. 16g). The mineral composition is nearly stoichiometric $PtAs_2$ but contains up to 0.33 wt.% Ag and up to 1.1 wt.% Au. Cooperite occur as idiomorphic crystals up to 7 μm in size (Fig. 16h) in an ultraheavy concentrate in the supra-ore zone from a sample containing 8.3 ppm Pt in a sulfide concentrate derived from aggregates of pyrite metacrystals with quartz margins. This sample of low-grade protore, containing 1 ppm Au, is characterized by elevated contents of Ag (11 ppm) and Ni (799 ppm) with Ni/Co = 7. Palladium is not incorporated in native platinum or gold but forms intermetallic compounds including a palladium silver tellurobismuthide, close to kotulskite–merenskyite, which occurs as intergrowths with galena and sphalerite. Minerals containing rhodium and other rare PGE also can be found in some parts of the deposit. This is shown by high Rh concentrations of up to 8 wt.% in an ultraheavy fraction of sample 109-241.

4.2.3. Platinum-group metals in carbon-rich concentrates

The relationship of PGM mineralization to carbonaceous matter is discussed in all publications about PGE mineralization in ores of the Sukhoi Log deposit. For example, the carbon-rich fractions (53–92 wt.% C_{org}) separated by Razvozzhaeva et al. (2002) contained 300–1000 ppm Pt. The concentrates were obtained by the following multistage procedure: decantation in water, dissolution in HCl to remove carbonates and some aluminosilicates, dissolution in HF to remove the other silicates and quartz, and dissolution in HNO_3 to remove sulfides. The residue was called "insoluble carbonaceous matter" and was strongly enriched in Pt. The initial samples contain 0.6–0.9 wt.% C_{org} and <0.03 ppm Pt. Thus, the residue concentrated PGM, which could be chemically bound with carbon or form PGM minerals such as to the acid-resistant phases found in our study.

The resultant concentrates were studied by transmission electron microscopy and electron diffraction, which indicated that organic matter to consist of both amorphous and crystalline graphite. X-ray photoelectron spectroscopy revealed Pt contents similar to those determined by Razvozzhaeva et al. (2002). According to studies of chemical bond energy, all platinum occurs as reduced metal. Scanning electron microscopy displayed hundreds of tiny native platinum crystals in the concentrate mainly as crystals 0.5–2 μm in size, but with a few individual grains as large as 10 μm (Fig. 17a). The very largest grains reach 30 μm but consist of aggregates of platy crystals, each of which is only a few tenths of a micrometer (Fig. 17b). Native Pt contains 98–99 wt.% Pt with tiny amounts of Cu and Fe (about 1 wt.%). Thus, the carbon-rich concentrate was enriched in the acid-resistant native platinum, but other important mineral phases were also discovered in the concentrates. We also discovered a Pt–Tl–Cl mineral. Although the mineral is too small to be analyzed quantitatively (Fig. 17c), semiquantitative analysis of its spectrum, based on X-ray peak heights, indicate a composi-

Fig. 17. Platinum minerals and native metals in carbon-rich concentrates of the Sukhoi Log deposit. Scanning electron microscope. The background is carbonaceous substance. (a) A plate of native platinum and its spectrum; (b) aggregate of native platinum plates and spectrum of platinum; (c) intergrowth of native indium with pyrite and spectrum of indium; (d) mineral PtTlCl4 and its spectrum. (Bar scale = 2 μm in all cases.)

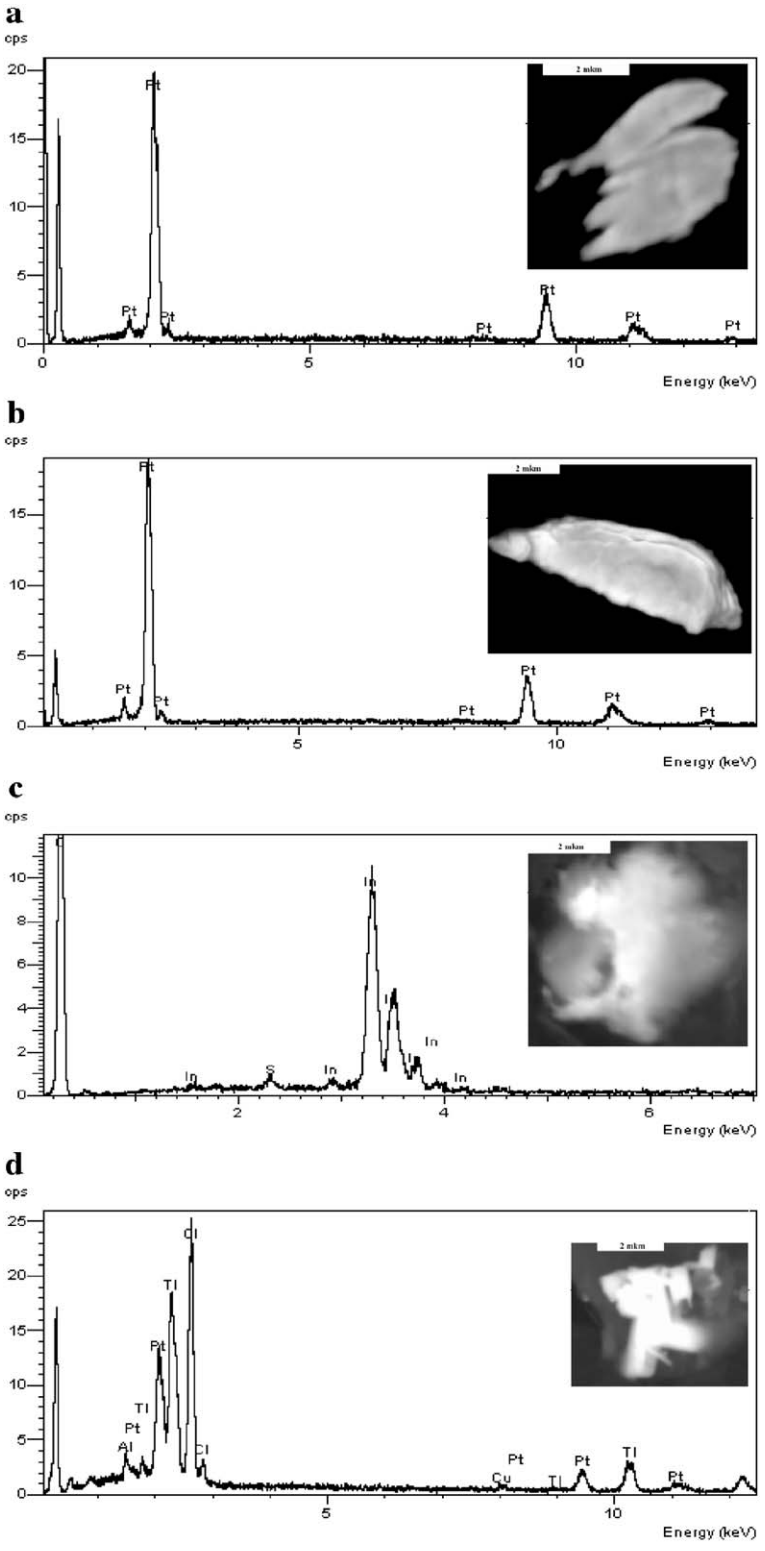
a
cps
Pt
Energy (keV)
b
cps
Pt
Energy (keV)
c
cps
In
S
Energy (keV)
d
cps
Cl
Tl
Pt
Al
Cu
Energy (keV)

tion near $PtTlCl_4$. Native indium is found as an intergrowth with pyrite (Fig. 17d). The concentrate also contains minor relics of pyrite, Co and Fe sulfoarsenides, rutile, xenotime, and molybdenite typical for mineralized shale. Rhenium sulfide (ReS_2) and native gold also are present.

5. REE geochemistry

5.1. Ree in black shale

Results of the REE analyses of whole-rock samples and gangue minerals (quartz and Fe–Mg carbonates) are given in Table 9. REE concentrations in the black shales exceed concentrations of the C1–chondrite standard with a pronounced enrichment in LREE and a negative Eu anomaly (Fig. 18a). Their range is close to the NASC standard (Taylor and McLennan, 1985). The NASC-normalized REE patterns show the same enrichment in LREE, a marked positive Eu anomaly, significant depletion of the middle REE (MREE) and a steep increase in Yb and Lu (Fig. 18b).

The total REE concentration in the mineralized zone is noticeably lower than in peripheral probably because of saturation of REE-deficient quartz–sulfide veinlets. The existence of similar REE whole-rock patterns for the supra-ore, infra-ore, and protore zones implies that REE were not redistributed during the mineralization.

5.2. REE in quartz

REE patterns for quartz normalized to NASC are shown in Fig. 18c. Such normalization regarding

Table 9
REE concentration (ppm) in bulk-rock samples, quartz, and carbonate of the Sukhoi Log deposit by ICPMS

Sample		La	Ce	Pr	Nd	Sm	Eu	Gd	Tb	Dy	Ho	Er	Tm	Yb	Lu	La/Lu_n
112 024	Bulk shale	21.30	45.70	5.58	21.70	4.57	0.90	2.72	0.25	1.14	0.20	0.66	0.12	0.99	0.19	12.01
112 052		20.90	44.60	5.55	21.70	4.44	0.88	2.60	0.25	1.14	0.19	0.62	0.11	0.87	0.16	14.00
112 062		21.60	46.30	5.62	22.10	4.57	0.85	2.78	0.28	1.29	0.22	0.70	0.13	1.07	0.19	12.18
112 080		14.90	31.00	3.86	14.90	3.06	0.68	2.13	0.23	0.98	0.20	0.53	0.11	0.80	0.14	11.41
112 096		11.60	24.40	3.04	11.80	2.76	0.68	2.09	0.21	1.03	0.20	0.55	0.09	0.75	0.13	9.56
112 122		15.70	32.10	3.90	15.20	3.22	0.66	2.12	0.24	1.00	0.18	0.06	0.11	0.93	0.16	10.52
112 150		12.80	26.80	3.30	12.70	2.88	0.63	1.95	0.20	0.97	0.19	0.57	0.09	0.79	0.15	9.15
112 164		18.80	39.70	4.89	18.50	3.95	0.82	2.55	0.25	1.22	0.20	0.63	0.11	0.93	0.17	11.85
112 180		14.10	29.00	3.50	13.40	2.75	0.62	1.79	0.17	0.92	0.16	0.49	0.10	0.90	0.15	10.07
112 204		19.30	41.90	5.12	20.10	4.06	0.86	2.55	0.27	1.21	0.21	0.63	0.11	0.94	0.18	11.49
112 220		22.40	47.00	5.74	21.90	4.28	0.84	2.69	0.30	1.23	0.21	0.68	0.11	0.95	0.15	16.00
112 236		19.80	41.70	5.08	19.20	3.71	0.71	2.24	0.23	0.99	0.18	0.56	0.12	0.80	0.15	14.15
Average (25)		15.94	33.45	4.06	15.58	3.20	0.67	2.06	0.21	0.97	0.17	0.50	0.09	0.78	0.14	12.36
36 090	Quartz	10.55	9.33	9.16	7.75	6.34	2.93	5.87	5.68	5.91	6.14	6.75	7.69	7.41	7.60	1.39
36 195		10.55	9.66	8.84	8.03	6.60	2.76	5.83	5.95	6.10	5.96	7.11	6.92	7.18	8.40	1.26
36 237		10.97	9.33	8.53	7.28	5.95	2.59	5.44	5.41	5.63	5.26	6.39	6.54	6.88	7.60	1.44
109 051		29.96	22.22	18.32	15.87	12.88	10.34	11.41	11.62	10.79	9.82	9.64	9.62	8.65	10.40	2.88
109 145		10.55	10.26	9.58	8.99	7.91	3.79	7.67	6.49	7.01	6.67	6.99	7.69	7.29	8.00	1.32
109 207		35.02	23.37	20.84	18.24	16.21	10.00	11.99	10.54	10.55	9.47	10.36	10.00	10.12	10.00	3.50
109 226		10.13	9.64	8.84	7.94	7.19	2.93	6.36	6.76	6.85	6.49	7.53	7.31	7.53	8.40	1.21
112 084		27.85	8.77	8.21	7.77	6.14	2.76	5.39	4.86	6.30	6.32	6.14	6.54	7.00	8.40	3.32
Average		18.20	12.82	11.54	10.24	8.65	4.76	7.49	7.16	7.39	7.02	7.61	7.79	7.76	8.60	2.12
109 051	Carbonate	16.33	12.43	11.16	10.73	15.36	27.07	14.08	11.35	7.72	5.09	4.34	3.85	3.35	4.00	4.08
36 090		8.10	7.89	7.58	7.86	7.32	4.83	4.85	3.51	3.31	3.33	4.58	6.15	8.94	10.80	0.75
36 237		4.39	4.44	4.53	5.14	6.08	5.17	5.87	4.59	4.21	3.86	4.94	6.54	8.76	11.20	0.39
112 038		60.34	50.98	40.74	33.40	20.07	10.69	9.85	6.49	4.29	3.68	4.58	6.15	8.65	11.60	5.20
112 195		19.79	15.74	12.00	10.19	7.39	5.17	5.78	4.59	4.02	4.04	4.82	6.92	9.94	12.40	1.60
Average		21.79	18.30	15.20	13.46	11.24	10.59	8.09	6.11	4.71	4.00	4.65	5.92	7.93	10.00	2.18

La/Lun—chondrite-normalized ratio.

genetically similar rocks gives a reversed slope of patterns with significant LREE depletion and negative Eu anomaly contrasting with whole-rock patterns. Although significant diodachy can be ruled out, quartz can incorporate REE in crystal structure defects, as REE mineral inclusions, and in fluid inclusions. REE-rich quartz samples from thick low-grade quartz veins display a Eu-maximum instead of a minimum and a notable negative Ce anomaly.

When the REE patterns are normalized to average Sukhoi Log black shales (Fig. 18d) the background REE distribution of the Khomolkho shales, the REE induced by hydrothermal mineralization is emphasized. These patterns show HREE enrichment with a negative Eu anomaly ranging from weak for vein quartz to strong for quartz from quartz–sulfide veinlets. The La/Lu_n ratio normalized to C1–chondrite probably reflects the degree of fractionation of LREE from HREE. For the quartz sample, this ratio is less than 1 and, according to Bau (1991), such data suggest that complex processes decreased REE solubility.

5.3. REE in carbonates

Except for one analysis, similar REE patterns exist for Fe–Mg carbonates although the range of values is much wider (Fig. 18e,f). All Fe–Mg carbonates demonstrate a pronounced enrichment in HREE with a Eu-maximum in one case and no Eu anomalies in other cases. The carbonates have LREE concentrations about an order of magnitude lower than black shale wall-rock and elevated HREE concentrations. Typically, REE enter carbonates replacing Ca, thus LREE (La^{3+} ionic radius $r = 1.03$ A) can more readily substitute for Ca^{2+} ($r = 1.06$ A) than HREE (Lu^{3+} $r = 0.86$ A) (Morgan and Wandless, 1980). For Mg–Fe carbonates, the process of replacement of Mg

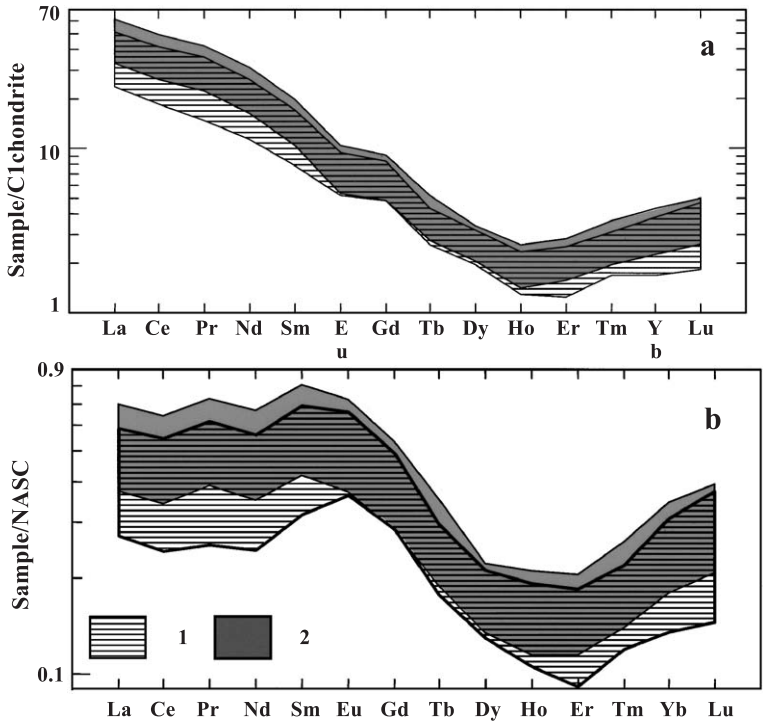

Fig. 18. REE patterns of altered rocks and ores of the Sukhoi Log deposit. (a) Chondrite-normalized REE patterns for black shale; (b) NASC-normalized REE patterns for black shale; (c) NASC-normalized REE patterns for quartz; (d) REE patterns for quartz normalized by wall black shale of the Sukhoi Log deposit; (e) NASC-normalized REE patterns for Fe–Mg carbonates; (f) REE patterns for Fe–Mg carbonates normalized by black shale wall rocks.

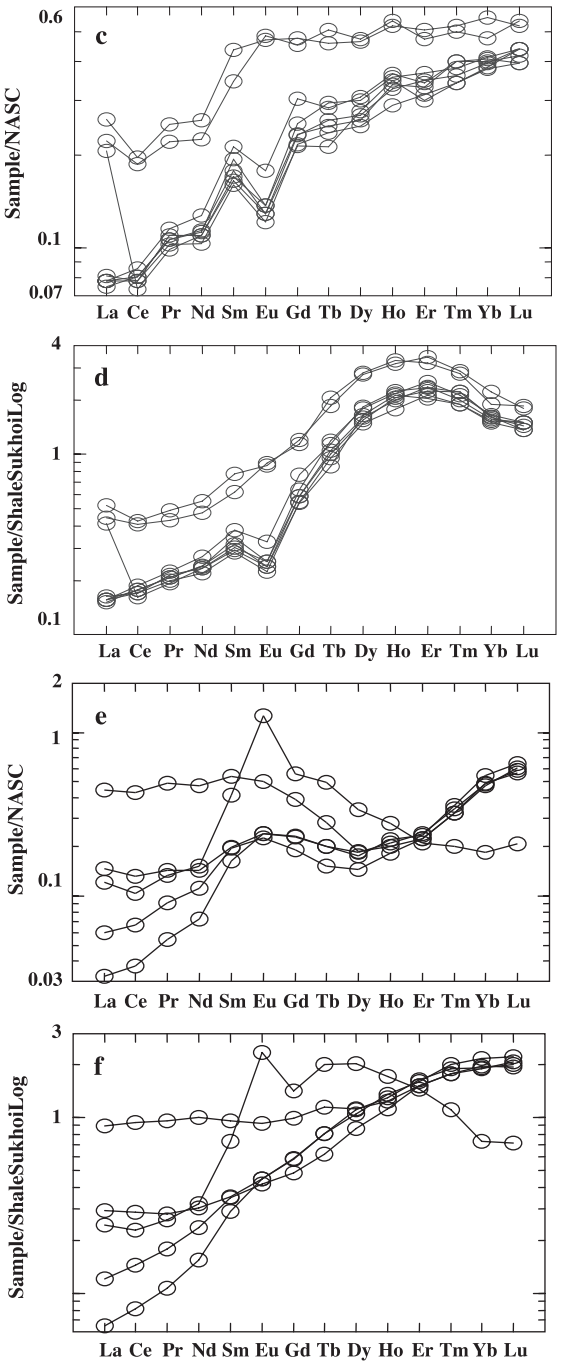

Fig. 18 (*continued*).

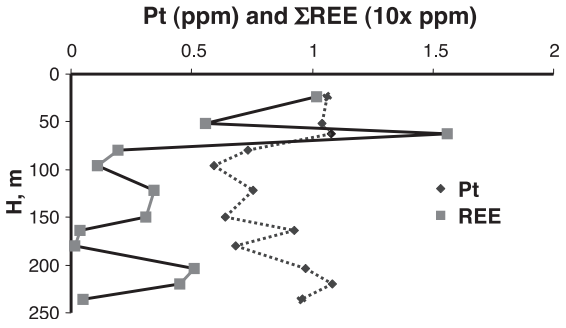

Fig. 19. Correlation between Pt contents and REE concentrations in drill core 112.

($r = 0.78$ A) by HREE having a smaller radii will dominate together with the replacement of calcium in ankerite. Therefore, significant enrichment in HREE can occur readily in carbonates. But HREE enrichment is also observed in coexisting quartz and probably reflects REE speciation in the ore-forming fluid.

In vertical sections of a few drill holes, there is a positive correlation between the sum of REE contents and platinum contents in the bulk sample (Fig. 19) possibly because of their simultaneous concentration in black shale during diagenesis or coeval deposition in the same paragenesis from hydrothermal fluid. No correlation between REE and Au or between Pt and Au were observed.

6. Organic matter

6.1. The composition and distribution of organic matter

The average contents of organic carbon in the altered host rocks of the Sukhoi Log deposit total about 0.5 wt.% ranging from 0.15 to 1.1 wt.% (Table 10). The total carbon content averages about 2.3 wt.%, so that the amount of carbonate carbon is two to four times larger than the amount of organic carbon. Significant amounts of nitrogen (from 0.08 to 0.19 wt.%) occur in the black shales of the Sukhoi Log deposit. Sulfur contents up to 20 wt.% reflect the intensity of mineralization.

Samples studied show no correlation between noble metal contents and organic carbon content (Fig. 15). Neither does gold correlate with sulfur.

Table 10
Partial chemical analyses (wt.%) and isotopic composition (‰) of black shales of the Sukhoi Log deposit

Sample	$\delta^{18}O_{carb}$	$\delta^{13}C_{carb}$	$\delta^{13}C_{tot}$	$\delta^{13}C_{org}$	Total C	Org. C	Carb. C[a]	H	N	S
36090	29.5	n.a.	n.a.	− 11.3	2.36	n.a.	n.a.	0.26	0.08	
36107	30.2	− 8.4	n.a.	− 19.9	2.33	n.a.	n.a.	0.25	0.09	0.5
36124	19.4	− 4.3	n.a.	− 16.6	3.1	n.a.	n.a.	0.24	0.1	0.31
36178	16.4	− 13.5	n.a.	n.a.	1.53	n.a.	n.a.	0.22	0.12	10.1
36200	18.2	− 5.0	n.a.	− 6.7	2.5	n.a.	n.a.	0.28	0.13	3.09
36233	29.0	− 6.1	n.a.	− 17.7	2.88	n.a.	n.a.	0.27	0.11	0.22
36245	29.7	− 5.0	n.a.	− 13.7	1.9	n.a.	n.a.	0.35	0.12	19.1
36287	n.a.	− 8.4	n.a.	− 16.2	1.53	n.a.	n.a.	0.37	0.12	0.61
36291	23.8	− 6.0	n.a.	− 13.2	1.37	n.a.	n.a.	0.41	0.12	0.73
112014	17.2	− 7.8	− 9.9	− 32.2	2.73	0.62	2.11	0.23	0.14	n.a.
112026	23.6	− 9.2	− 11.5	− 34.9	2.46	1.12	1.34	0.22	0.15	n.a.
112038	18.0	− 24.9	− 9.8	− 17.4	2.4	0.43	1.97	0.23	0.15	n.a.
112052	19.7	− 25.6	− 12.2	− 21.7	2.45	0.4	2.05	0.21	0.16	n.a.
112064	28.5	− 8.6	− 9.9	− 25.4	2.37	0.68	1.69	0.22	0.16	n.a.
112084	21.5	− 15.5	− 8.3	− 27.8	2.84	0.43	2.41	0.23	0.16	n.a.
112102	20.0	− 19.1	− 9.5	− 22.9	2.55	0.48	2.07	0.22	0.17	n.a.
112110	29.8	− 7.2	− 5.9	− 20.2	2.3	0.37	1.93	0.23	0.17	n.a.
112120	24.5	− 9.8	− 20.4	− 42.0	2.25	0.45	1.8	0.23	0.18	n.a.
112140	24.8	− 8.1	− 7.7	− 18.3	2.47	0.35	2.12	0.24	0.16	n.a.
112150	21.6	− 21.3	− 21.3	− 16.4	2.43	0.15	2.28	0.25	0.18	n.a.
112160	26.0	− 11.5	− 11.7	− 15.0	2.44	0.71	1.73	0.27	0.19	n.a.
112184	23.5	− 17.3	− 13.1	− 32.5	2.75	0.61	2.14	0.23	0.17	n.a.
112204	16.5	− 3.4	− 19.5	− 40.6	1.42	0.35	1.07	0.33	0.18	n.a.
112224	22.3	− 11.9	− 10.6	− 25.5	1.91	0.44	1.47	0.32	0.15	n.a.
112236	29.5	− 12.6	− 11.3	− 22.4	1.84	0.55	1.29	0.33	0.16	n.a.
Average	23.5	− 11.0	− 12.0	− 22.1	2.28	0.51	1.84	0.27	0.14	4.3

n.a.—not analysed; blank—not detected.
[a] Carbonate C content = total C content − organic C content.

6.2. Insoluble carbon-bearing matter

Insoluble carbon-bearing matter occurs in the wall rocks as a dispersed phase corresponding to a disordered or cryptocrystalline graphite. The organic matter is dominated by kerogenous material resembling graphite that does not contain functional groups and that originated during the metamorphism. Oxidation of these phases begins at 450–550 °C corresponding to the conditions of greenschist facies metamorphism.

The ash-free concentrates contain 95 wt.% of carbon, 1.4 wt.% of hydrogen, and 3.4 wt.% of total nitrogen, sulfur, and oxygen. The electron microscope data show the existence of the two morphological types of insoluble carbon matter, aggregates of droplets (dendritic form), and cellular aggregates (sorbed form).

To estimate the limits of sorption or some other type of incorporation of noble metals, we separated concentrates of the graphite-like material and found that some fractions of insoluble organic matter contain up to 10 ppm of Au and PGE. The mode of incorporation of noble metals into insoluble carbonaceous matter was investigated using Auger spectroscopy and X-ray photoelectron spectroscopy. The X-ray photoelectron spectroscopy indicates that gold occurs in carbon as a noncharged form (Au^o), suggesting that gold exists in the native form, as ultrafine particles that are sorbed on the surface of the carbon. This could also be true for platinum group elements, but PGE concentrations, which were lower than the detection limits of the analytical methods (0.01 wt.%).

6.3. Soluble organic matter

Soluble organic matter (bituminoids) could be of greatest interest as a possible concentrator of noble metals with organic ligands. Total contents in samples from protore, supra-ore, and infra-ore zones of the deposit are 9, 10, and 8 ppm, respectively. Phase composition of the soluble organic matter was ana-

lyzed by chromatography mass spectrometry, which revealed the following organic compounds:

(a) *Protore zone*—nonbranched saturated hydrocarbons (C_{15}, C_{17}, C_{19-21}, C_{23}, C_{24}, C_{36}); ethyl esters of carboxylic acids (C_{14}, C_{18}, phthalates); high-molecular compounds ($C_{12}H_{17}$, C_5H_{44}, $C_{21}H_{44}$, $C_8H_{34}0_8$); amides.

(b) S*upraore zone*—nonbranched saturated hydrocarbons (C_{14-19}, C_{21-25}, $C_{24}H_{50}$); branched saturated hydrocarbons (tetramethyl C_{15}); ethyl esters of carboxylic acids (C_{16}, C_{18}); phthalates (dimethylphthalate).

(c) *Infraore zone*—nonbranched saturated hydrocarbons (C_{15}, C_{17-20}, C_{23}, C_{24}, C_{26}); branched saturated hydrocarbons (dimethyl C_{13}, tetrameth-

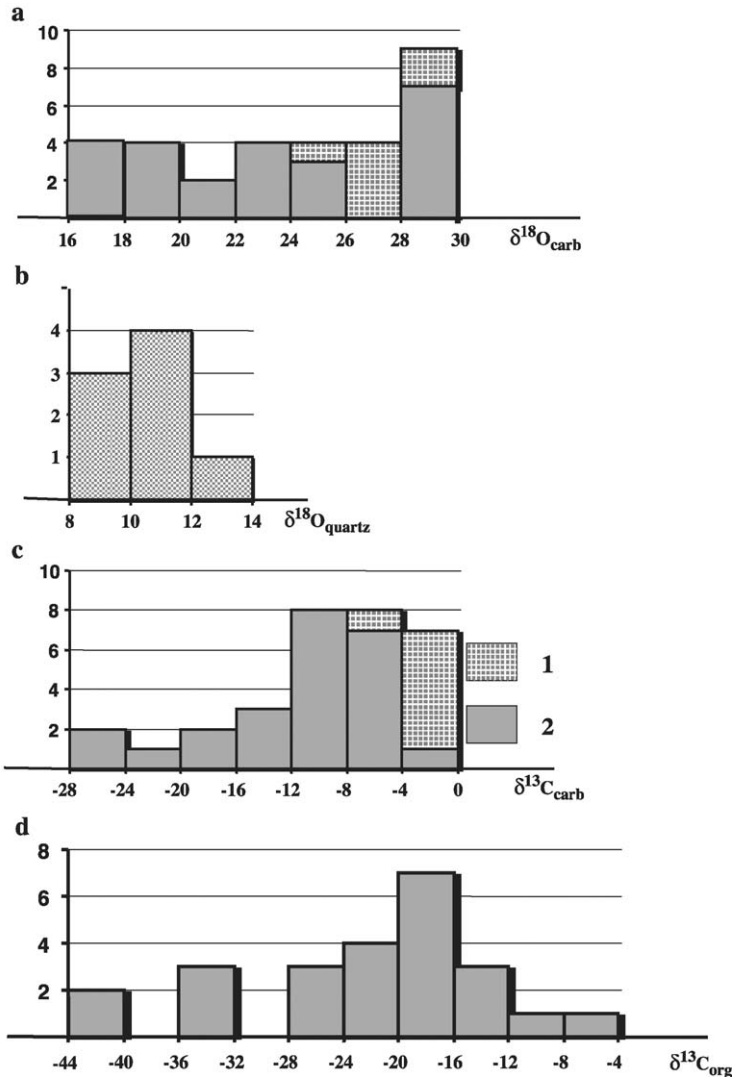

Fig. 20. Histograms of isotopic composition of oxygen and carbon in Sukhoi Log ores. (a) Gray = $\delta^{18}O$ values of carbonate matter in black shale and Waffle pattern = Fe–Mg carbonates; (b) $\delta^{18}O$ values in quartz; (c) Waffle pattern = $\delta^{13}C$ values of carbonate matter in black shale and Gray = Fe–Mg carbonates (2); (d) $\delta^{13}C$ values of organic matter in black shale.

yl C_{17}, carboxylic acids C_9, C_{16}); ethyl esters of carboxylic acids (C_{11}, C_{14}, C_{18}); phthalates (dimethylphthalate, diethylphthalate, dibutylphthalate); high-molecular compounds (C_5H_4NS, $C_{12}H_{17}ON$, $C_{21}H_{44}$, $C_{18}H_{34}O_4$); amides.

All samples contain molecular sulfur S_8 and S_6 with S concentrations of $1 \cdot 10^{-4}$ g/l. The less variable composition of soluble organic matter is typical of the protore and this is possibly related to intense hydrothermal alteration in this zone.

The identified organic compounds (amides, high-molecular compounds, and others) could form complexes with noble metals. However, only volatile compounds of mercury, arsenic, and silicon were found in chloroform bituminoids, whereas complexes with noble metals were not detected.

The gas phase is composed of non-hydrocarbon (CO_2, N_2, H_2) and light hydrocarbon (CH_4 and C_2H_6) components with total contents of volatile phases up to 10 mol/kg.

7. Stable isotopes

7.1. Carbon and oxygen isotopic composition

The $\delta^{13}C_{carb}$ values of 31 bulk-rock samples range from −3.4‰ up to −28.6‰, PDB (Table 10). Samples from supra-ore, infra-ore, and protore zones of $\delta^{18}O_{carb}$ values of 30 bulk-rock samples are less divergent ranging from 16.4‰ to 30.2‰, SMOW with a mean value of about 23.5‰ (Fig. 20). The variability is not systematic and there is no obvious difference between the three zones. The oxygen isotopic composition of Sukhoi Log black shale is close to the isotopic composition of marine carbonates (Faure, 1986). However, the $\delta^{13}C_{carb}$ and $\delta^{18}O_{carb}$ values for black shale differ from typical marine shale values.

The $\delta^{13}C_{carb}$ values for Fe–Mg carbonates range from −0.12‰ to −6.17‰ (Table 11). Ankerite porphyroblasts have the heaviest carbon isotopic composition. Mg-rich siderite from quartz–sulfide veinlets has characteristically narrow ranges of variation averaging −2.5‰. The $\delta^{18}O_{carb}$ values of Fe–Mg carbonates vary from 24‰ to 30‰. Values for quartz from quartz–sulfide veinlets range only from 8.8‰ to 13.5‰.

Table 11
Isotopic composition of Fe–Mg carbonates and quartz (‰) from altered black shales and ores of the Sukhoi Log deposit

Sample	Mineral association	$\delta^{18}O_{quartz}$	$\delta^{13}C_{carb}$	$\delta^{18}O_{carb}$
112038	Siderite porphyroblasts		−1.1	27.3
36237	Siderite–quartz–sulfide veinlets	9.9	−6.1	24.2
36195	Siderite–quartz–sulfide veinlets	10.9	−2.6	26.9
36090	Ankerite porphyroblasts and quartz–sulfide veinlets	11.6	−0.1	27.7
6/237	Siderite–quartz–sulfide veinlets		−2.1	29.8
6/237	Siderite–quartz–sulfide veinlets		−1.5	27.8
8/203	Siderite–quartz–sulfide veinlets		−2.8	29.7
109051	quartz–sulfide veinlets	11.4		
109127	quartz–sulfide veinlets	10.5		
109145	quartz–sulfide veinlets	8.8		
109207	quartz–sulfide veinlets	9.6		
112084	quartz–sulfide veinlets	13.5		

Blank—not analysed.

7.2. Isotopic composition of organic carbon

The $\delta^{13}C_{org}$ values for organic carbon range from −6.7‰ to −42‰ with most values in the interval from −10‰ to −20‰ and a mean value of about −22‰ (Table 10, Fig. 20). Four kerogen-enriched fractions were studied by consecutive dissolution of carbonaceous, silicate, and sulfide components of the black shales. The $\delta^{13}C_{org}$ values of kerogen-enriched fractions range from −17.9 to 25.4 also with a mean value of −22‰. The great variation for reduced carbon may reflect intensive isotopic exchange reactions between organic matter and carbonates.

7.3. Sulfur isotopic composition of sulfides

The $\delta^{34}S$ values in pyrite range from +3.5‰ to +15.3‰ CDT for 15 samples. Pyrite from quartz–sulfide veinlets has uniform $\delta^{34}S$ values within all mineralized bodies of the deposit ranging from +8.0‰ to +11.1‰ with a mean of +9‰. Sedimentary pyrite has $\delta^{34}S$ of 3.5‰ and isotopically light sulfur is probably connected with bacterial reduction or the decomposition of S-bearing organic matter. Pyrite from the thick quartz veins has the highest $\delta^{34}S$ values of about +15‰.

Table 12
The basic parameters of mineralization and ore-forming fluid (evidence from fluid inclusions)

Type of mineralization	Mineral, type of inclusion	Temperature, °C (number of inclusions)	Pressure, bar	P_{total}/P_{H_2O}	C salts, wt.%, NaCl equiv.	C_{CO_2}	C_{CH_4}	CO_2/CH_4	Composition of vapor phase
Quartz–sulfide veinlets	Quartz (3, 4)	385–185 (334)	2290–200	70.6–2.9	8.6–5.3				N_2
	Quartz (1, 2)	350–210 (184)	2370–190	54.0–1.03	8.1–5.6	7.6–1.8	1.1–0.3	1.1–1.9	CO_2, CH_4, N_2
	Quartz (5)	335–130 (147)			9.5–3.7				CO_2
	Carbonate (1, 2)	340–280 (24)	1780–1560	13.3–13.2	6.7–5.0	6.7–5.3	1.0–0.7	8.0–6.0	CO_2, CH_4, N_2
	Carbonate	205–185 (24)			6.3–5.5				
Quartz vein	Quartz (1, 2)	385–275 (214)	2450–130	22.3–1.6	7.6–5.8	7.0–2.1	1.0–0.5	8.6–2.1	CO_2, CH_4, N_2
	Quartz (5)	210–185 (42)			7.6–5.4				

Types of inclusions (see text): (1) gas-saturated $N_2–CH_4–CO_2$ inclusions; (2) vapor $N_2–CH_4–CO_2$ inclusions; (3) vapor–liquid inclusions; (4) vapor inclusions with dense nitrogen; (5) vapor–liquid inclusions of diluted solution.

Thus, the tendency for ^{32}S depletion is observed for the various subsequent generations of pyrite, but the hydrothermal ore-bearing fluid had a fairly homogeneous sulfur isotope composition.

8. Fluid inclusions

8.1. General characteristics

Primary and pseudosecondary inclusions 3–25 μm in size occur mainly as negative crystals in quartz and carbonate minerals. The concentration of inclusions in selected growth zones and location of inclusions in the shadows solid phases were used as the principal criteria for primary origin (Roedder, 1984). Studies focused on primary inclusions entrapped initially from homogeneous environment. However, some inclusions consist of two phases (liquid + vapor) suggesting the possibility of boiling hydrothermal fluids.

The fluid inclusions were divided into five compositional types. Type 1—gas-saturated, consisting of an aqueous solution and a dense $N_2–CH_4–CO_2$ gas; type 2—vapor-rich, containing a dense $N_2–CH_4–CO_2$ gas mixture, syngenetic with type 1; type 3—two-phase vapor-rich inclusions containing aqueous solution and sometimes nitrogen gas phase; type 4—vapor-rich inclusions filled with dense nitrogen and syngenetic to type 3; type 5—two-phase inclusions of dilute solution entrapped from homogeneous fluid. No vapor inclusions syngenetic to type 5 were found.

Fluid inclusions were investigated using cryometric and thermometric methods. In the experiments, large groups of compositionally uniform inclusions differing in size were selected because the smallest inclusions are less likely to be damaged. Heating preceded freezing to avoid the possibility of destruction for inclusions from high internal pressure.

Microthermometric studies were carried out on a THMSG-600 Linkam stage, allowing measurement of temperatures of phase change from −196 to 600 °C and observation at high magnifications. Fluid inclusion salinities for types 3 and 5 were estimated from ice melting temperatures (Bodnar and Vityk, 1994). It was not possible to determine salinities for type 1 fluid inclusions containing dense $CO_2–CH_4$-rich fluid on the basis of clathrate melting temperature (Collins, 1979; Darling, 1991). In this case, the clathrate melting temperature was above +10 °C due to the high methane content. The salinity was obtained from the ice melting temperature, and corrected on the basis of measurement of the volumetric proportions of CO_2 and H_2O phases and calculation of carbonic acid concentrations in solution. Concentration of methane was estimated on the basis of volumetric proportions and methane's density connected with its partial pressure, which in turn determines methane's clathrate

Fig. 21. Plots of fluid inclusion data: (a) salinity vs. temperature; (b) pressure vs. temperature; (c) P_{total}/P_{H_2O} ratio vs. pressure in hydrothermal system of the deposit. Open circles—storkwork quartz–sulfide veinlets mineralization; solid circles—thick quartz vein; Wb—the compositional field of solution for the Waterberg deposit by the evidence for fluid inclusion (Distler et al., 2000).

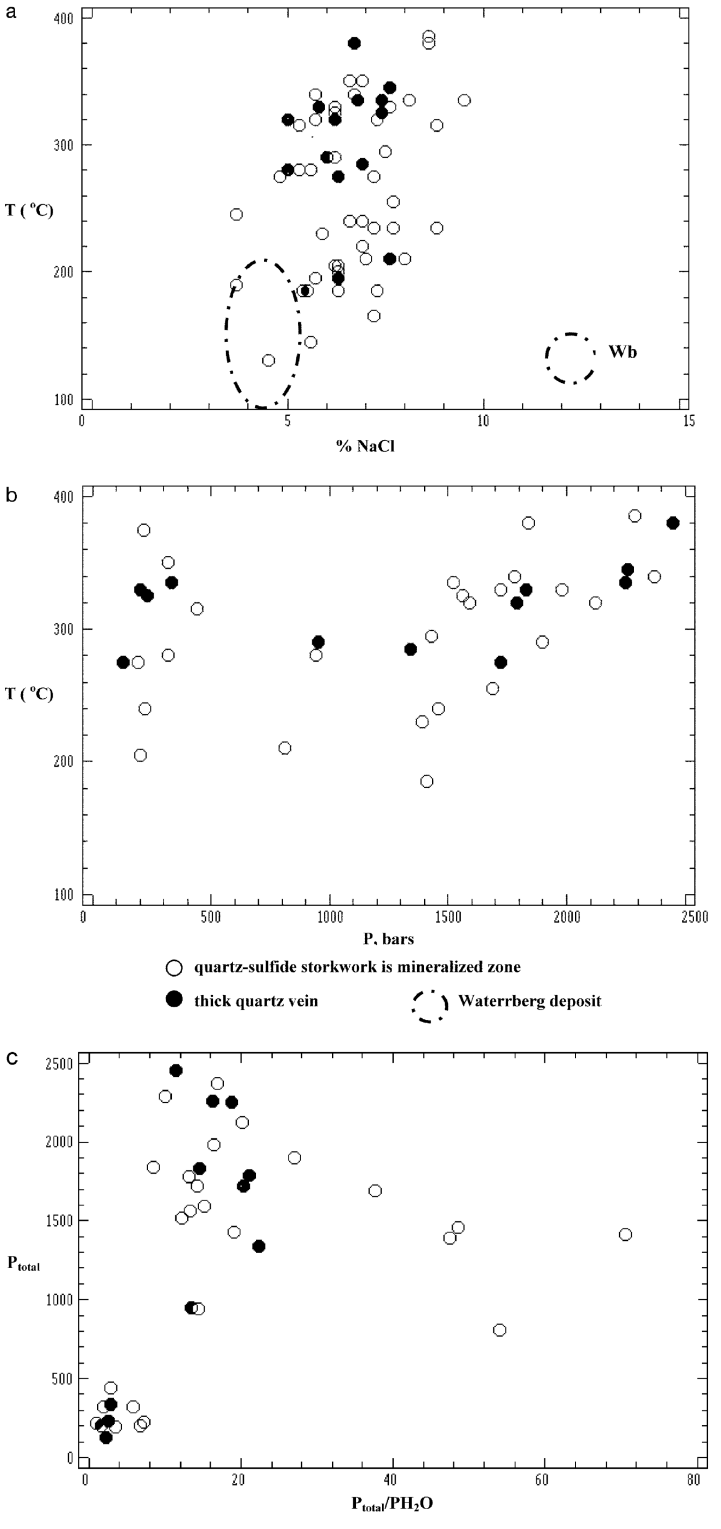
a
T (°C)
% NaCl
Wb
b
T (°C)
P, bars
quartz-sulfide storkwork is mineralized zone
thick quartz vein
Waterrberg deposit
c
P_{total}
P_{total}/PH_2O

melting temperature (Claypool and Kaplan, 1974). On the basis of these data, the necessary corrections for the amount of gas hydrate water were used to estimate the salinity of the CO_2–CH_4–H_2O-rich fluid, leading to good approximations of (± 0.5%) salinities.

Pressure of the heterogeneous fluid was derived as the sum of vapor pressure and pressure of dense gases (CO_2, CH_4, N_2) in vapor-rich and vapor–liquid inclusions. Estimation of salinity, densities of CO_2–CH_4 mixtures and N_2, and also their pressures was carried out using the FLINCOR program (Brown, 1989; Brown and Lamb, 1989). Construction of isochores and estimation of pressure in CO_2–CH_4-rich inclusions utilized the data of Kerkhof (1988) and Thiery et al. (1994).

Element concentrations in aqueous extracts from four samples of ore-bearing quartz were analyzed using VG-Plasma Quad 2 ICPMS. The extracts were obtained from aggregates of quartz grains 0.5–0.25 mm in size and 10–15 g in weight. A background solution was prepared before opening the inclusions, and thermal destruction was carried out at 450 °C with parallel determination of water by P_2O_5 sorption. The bulk solutions of both sample and background were identical and compounded 30–45 ml with 1:3 dilutions. Element contents were calculated as the difference of concentrations and were recalculated on the mass of solution.

For some inclusions, pressures were estimated on syngenetic essentially vapor-rich and vapor–liquid inclusions trapped from the heterogeneous ore-forming fluid using the isochore (on the vapor-rich inclusions) and isotherm (on the liquid-rich inclusions) intersection method (Kalyuzhny, 1982). Brown's (1989) program, FLINCOR, was utilized for pressure calculation.

8.2. Fluid inclusion data

The results of the thermometric and cryometric study of individual fluid inclusions in quartz and carbonate are given in Table 12. The inclusions display a wide range of basic physico-chemical parameters: homogenization temperature 130–385 °C, pressure 130–2450 bar, salinity 3.7–9.5 wt.% NaCl equiv., CO_2 concentration 1.8–7.6 m, CH_4 concentration 0.3–1.1 m, density of aqueous solution − 0.65 to 1.09 g/cm^3, $(P_{H_2O}+P_{gas})/P_{H_2O}$ 1.0–70.6. Magnesium, potassium, and sodium chlorides are the dominant dissolved salts judging from the eutectic temperatures of − 25 to − 34 °C.

Table 13
Element concentration in fluid inclusion solution measured by ICPMS

Element	Concentration, g/kg H_2O			
	2/198	6/237	36/72	6-198.2
Li	0.000843	0.000319	0.00105	0.01145
Be		0.000028	0.000075	0.00005
B	0.0028	0.001946	0.001275	0.0067
Na[a]	n.d.	n.d.	3.937	3.100
Na	n.d.	n.d.	2.497	2.080
Mg	n.d.	n.d.	0.135	3.145
Al	n.d.	n.d.	0.007425	0.0445
Cl	n.d.	n.d.	7.732	8.159
K[a]	n.d.	n.d.	1.147	0.920
K	n.d.	n.d.	0.420	0.960
Ca	n.d.	n.d.		8.040
Sc	0.00033	0.000169	0.00045	0.0018
V	0.000051	0.00007		0.0007
Cr	0.000089	0.00017	0.00164	0.00325
Mn	0.00099	0.00126		
Co			0.002325	
Ni	0.00025	0.000104	0.002925	
Cu			0.0009	0.0014
Zn	0.00149	0.00386	0.1515	
Ge			0.0043	
Ga	0.000019	0.000017		
Se			0.00132	0.0013
Rb			0.00083	0.00085
Sr	0.00769	0.00292	0.01515	0.04865
Mo	0.00005	0.00057	0.00023	0.0004
Ag	0.000018	0.000015	0.009525	
Sn			0.0003	
Sb	0.000266	0.000043	0.00015	
Cs			0.00045	0.00015
Ba	0.00215	0.00153	0.0285	0.01585
La	0.0074	0.0127	0.0912	0.0003
Ce			0.00023	0.0001
Pr			0.00004	0.000005
Nd			0.00015	0.000035
Gd			0.00004	0.000025
W	0.00053	0.000564		0.00045
Au		0.000003		0.0000125
Pb		0.000065	5.12226	0.00325
Bi			0.00031	0.00008
Weight, g	14.0141	9.76025	14.494	15.0003
Volume of solution, ml	42.00	30.00	43.48	45.00
Amount of H_2O, g	0.01528	0.01064	0.0058	0.0090

n.d.—not determined; blank—not detected.
[a] Concentration determined by titration.

Among vapor-rich inclusions, as already noted, two types can be distinguished—dense nitrogen inclusions (0.09–0.57 g/cm^3) with minor CO_2 (3–5 mol%) and N_2–CH_4–CO_2 inclusions (CO_2 = 70–90 mol%, CH_4 = 3–15 mol%, N_2 = 7–15 mol%). Such phase heterogeneity suggests that gases from two different sources and the low permeability of the host rock precluded the homogeneous mixing of different gases in the ore-forming system (Fig. 21). In fact, nitrogen-rich inclusions are connected with elevated $(P_{H_2O}+P_{gas})/P_{H_2O}$ ratios. It should be noted that dense nitrogen-rich inclusions were found only in the quartz–sulfide veinlets and not in the quartz veins, where heterogeneous N_2–CH_4–CO_2–H_2O inclusions dominate. In general, quartz veins were formed under more open conditions ($(P_{H_2O}+P_{gas})/P_{H_2O}$ ratio of 1.6 to 22.3) than quartz–sulfide veinlets ($(P_{H_2O}+P_{gas})/P_{H_2O}$ ratio of 1.03 to 70.6). At the same time, the higher $(P_{H_2O}+P_{gas})/P_{H_2O}$ ratio can be explained by the thermal decomposition of organic nitrogen-bearing matter (Laverov et al., 2000b).

Analysis of aqueous extracts by ICPMS (Table 13) has shown Cl, Na, K, Ca, and Mg to be the basic components of the inclusions. Also detected were: Au, Ag, Pb, Zn, Sb, Be, B, Mn, V, Cr, Ni, Li, Sr, Ba, Mo, W, Sc, Ga, and La in concentrations appropriate for endogenous fluids.

9. Discussion and genetic model of deposit

Whether or not carbonaceous rocks are a necessary or sufficient factor in the formation of noble metal deposits in black shales is a major question. Although metamorphosed sedimentary-carbonaceous formations are distributed regionally, economic mineralization only occurs locally. For example, the Bodaibo synclinorium contains only one major noble-metal lode despite the presence of widespread black shales.

Geological data indicate that Au mineralization was controlled by a tectonic zone along the anticlinal axis. The observed mineralization zoning is typical of infiltration metasomatism: early mineral assemblages are best preserved along the flanks, while late minerals predominate in the central ore zone that was most intensively altered by metasomatism.

Many metallogenic elements were found in the deposit: Au, Ag–Fe, Ni, Co, Cr, Ti, Pt, Pd–Zn, Cu, Pb–Sn, W, REE, and Zr. At least two geochemical assemblages can be distinguished, comprising metallogenic elements that usually do not occur together: the Fe–Ni–Co–Cr–Ti–Pt–Pd assemblage is typical of mafic and ultramafic rocks whereas the Sn–W–REE–Zr assemblage typifies granitoids. The central zone of the protore body is gold-rich, while its periphery is enriched in PGE, which may reflect changes in pH conditions and related Eh potential. In the early stage, most metals were deposited as native metals or intermetallic compounds, then as sulfosalts and, in the final stage, as sulfides. The assemblage of native metals includes native gold, native platinum, Pt–Fe–Cu alloys, and such exotic minerals as native chromium, iron, and tungsten, and alloys of Sn and Sb, and Ni and Sb. Native metals developed under the highly reducing conditions that were controlled by sulfur activity. We analyzed minerals of the pyrrhotite group and found that their composition varied from S-poor troilite, which occurs with ferroan pentlandite to S-rich monoclinic pyrrhotite, which occurs with nickeloan pentlandite. The nickeloan pentlandite occurs in equilibrium with millerite, heazlewoodite, and several thiospinels. The latest mineral pyrite contains relict inclusions of all of the other minerals in this sequence.

Studies of carbon and its isotopic fractionation facilitate an understanding of ore formation. Bulk carbon concentrations do not vary significantly throughout protore, except for intensely silicified sections; however, the mode of carbon occurrence varies. For example, intense carbonatization is observed in the mineralized zone where magnesium-rich, calcium-free carbonates of the ankerite–siderite series that probably result from the hydrothermal oxidation of organic carbon are abundant. It should be noted that various carbon species cause different effects in the ore-forming process. For instance, the oxidation of the graphitic matrix can directly result in carbonatization of decomposed Fe–Mg silicates.

Beside graphitic material, black shales contain soluble organic matter containing C–H and C–O–H functional groups which release CO_2, H_2O, and free hydrogen when thermally or chemically decomposed.

Consequent local reducing reactions can lead to the generation of native metals.

Alteration of carbonaceous matter is implied by carbon-isotopic data. The average composition of unaltered organic matter from the Sukhoi Log black shales is about −25‰, close to the isotopic composition of typical Precambrian sedimentary organic matter. Metamorphism favors retention of heavier carbon-isotopes, because of loss of compounds such as CH_4 that are enriched in light carbon (Watanabe et al., 1997); hence, original carbonaceous matter in the Sukhoi Log rocks was probably isotopically lighter than those analyzed. The carbonaceous matter could also change its isotopic composition in isotopic exchange with the carbon bonded in carbonates. Bulk carbon-isotopic compositions of Sukhoi Log black shales and carbonates differ from of marine carbonates. Probably, most of the Sukhoi Log carbonates were generated by organic carbon oxidation during processes of ferromagnesian metasomatism and metamorphism. However, the light organic carbon fractionation is unlikely to have been sufficiently intense to form the isotopically heavy hydrothermal siderite (average $\delta^{13}C_{carb}$ −2‰) found in quartz–sulfide veinlets which may have been deposited by processes unrelated to diagenesis and metamorphism.

The carbon-isotopic data for siderite from quartz–sulfide veinlets and porphyroblasts were used to calculate the isotopic composition of the hydrothermal fluid using the equation of Carothers et al. (1988) at a temperature N 200 °C:

$$1000\ln\alpha\ (\mathrm{Sid}-\mathrm{CO_2}) = 4.34{*}10^6{*}T^{-2} - 1.1{*}10^4T^{-1} + 6.82$$

Considering $1000\ln\alpha = (\alpha-1){*}1000 = \Delta(\mathrm{Sid}-\mathrm{CO_2})$ and extrapolating this equation to temperatures over 300 °C, we infer the isotopic fractionation between siderite and hydrothermal fluid to be less than 1‰. The isotopic compositions of siderite and fluid are similar at temperatures of about 380 °C, close to the maximum temperature for ore formation. For the hydrothermal fluid to be in equilibrium with siderite (sample 112038: $\delta^{13}C_{carb}$ −1.1‰ and $\delta^{13}C_{org}$ −24.9‰) at a temperature of 200 °C, the isotopic composition of CO_2 is estimated as −3.8‰ with $\Delta(\mathrm{Sid}-\mathrm{CO_2}) = 2.74$‰.

For the same fluid, we calculated the isotopic composition at graphite–CO_2 equilibrium, using the equation in Bottinga (1969):

$$1000\ln\alpha(\mathrm{CO_2}-\mathrm{Gr}) = 2.612{*}10^6{*}T^{-2} + 7.67{*}10^3T^{-1} - 4.86$$

We obtained a value of −2.5‰ for $\Delta(\mathrm{CO_2}-\mathrm{Gr}) = 22.4$‰. Thus, in the mineral assemblage considered, we believe the fluid also to be in equilibrium with carbonaceous matter that is common for this type of fluid (Bierlein and Crow, 2000).

Carbonate porphyroblasts could be formed in the process of more active oxidation of volatile and soluble organic fractions. This process can also explain the fact that some analyzed samples are enriched in ^{12}C. However, in most cases, the equilibrium between fluid and carbonaceous matter does not seem to have been reached. The fluid composition calculated on the siderite–CO_2 equilibrium at 200 °C is about 4.7‰ (average $\delta^{13}C_{carb} = -2$‰). Nevertheless, considering the average $\delta^{13}C_{org}$, we calculated that the $\delta^{13}C$ of fluid in equilibrium with carbonaceous matter to be near zero.

Thus, isotopic compositions provide evidence for two sources of carbon. Probably, the oxygen of sedimentary rocks did not influence the fluid composition significantly; hence, hydrothermal quartz and carbonate are characterized by a fairly homogenous oxygen-isotopic composition related to that of the hydrothermal source.

Variations in acidity and alkalinity of the mineralizing fluid were accompanied by major changes in the behavior of rare-earth elements. REE fractionation may be related to differences in the ionic radii of light and heavy REEs. The REE distribution and formation of Ce and Eu anomalies can be considered in terms of redox conditions in the solution, influences of the primary host-rock composition and compositions of hydrothermal solutions.

The Sukhoi Log deposit show similar REE patterns in the protores and altered rocks, being enriched in LREE, depleted in Tb–Tm, and slightly enriched in Yb and Lu. However, hydrothermal quartz and carbonates are enriched in HREE relative to LREE. Thus, the data indicate two general types of REE fractionation. According to Bau (1991), the $(La/Lu)_n$ ratio reflects the dominance of the complexation at (La/

$Lu)_n < 1$, and predominance of the sorption at $(La/Lu)_n > 1$. Consequently, the REE patterns for shales suggest a significant role for REE sorption during sedimentation whereas the REE patterns formed during hydrothermal activity were generally controlled by formation of complex minerals.

REE fractionation in carbonates reflects REE isomorphic incorporation into Fe–Mg carbonates. REE incorporation into quartz is not likely to be related to isomorphic substitution. Monazite in the metamorphosed black shales and in ore mineral assemblages concentrates a significant amount of REE. It is overgrown by Nd-rich phases with elevated contents of MREE and HREE suggesting a high mobility of these elements during precipitation of PGE minerals that is reflected by correlation between REE and PGE contents at Sukhoi Log. Data for REE in modern hydrothermal fluids show that complex formation is important REE mobility in fluids (Douville et al., 1999). In acid fluids, F^- and Cl^- form the strongest ligands with REE.

Mineralization for the Sukhoi Log deposit resembles that of the Waterberg hydrothermal PGE–Au deposit in South Africa (Distler et al., 2000). Temperatures up to 385 °C and similar mineral paragenesis dominated by native platinum and monazite occur. At least two types of fluid (low and high salinity) coexisted in both deposits (McDonald et al., 1995) as reflected by a distinct clustering of fluid compositions into two groups for the Waterberg deposit and evidence for heterogeneous mixing for the Sukhoi Log deposit in the temperature versus salt concentration diagram (Fig. 22).

The mineralizing processes were characterized by a complex interaction of endogenous hydrothermal fluids saturated in CO_2 and N_2 with organic matter of the host black-shale sequences. Mineralized material had at least two sources. Decomposition of the organic matter in the host rocks provided a reducing geochemical barrier, where the complexes of ore and noble metals decomposed due to changes in redox conditions, pH, and/or Eh and precipitated native metals and sulfides. Thermodynamic data show that Au can occur in the solution as $AuHS^0$, $Au(HS)_2^-$, and chloride complexes (Gammons and Williams-Jones, 1997; Symonds and Reed, 1993). Platinum forms complex compounds with Cl, C, and N, H_2PtCl_6, $PtCl_2$, and $(NO)_2PtCl_6$ and other complexes that occur in aqueous solutions (Gammons, 1995).

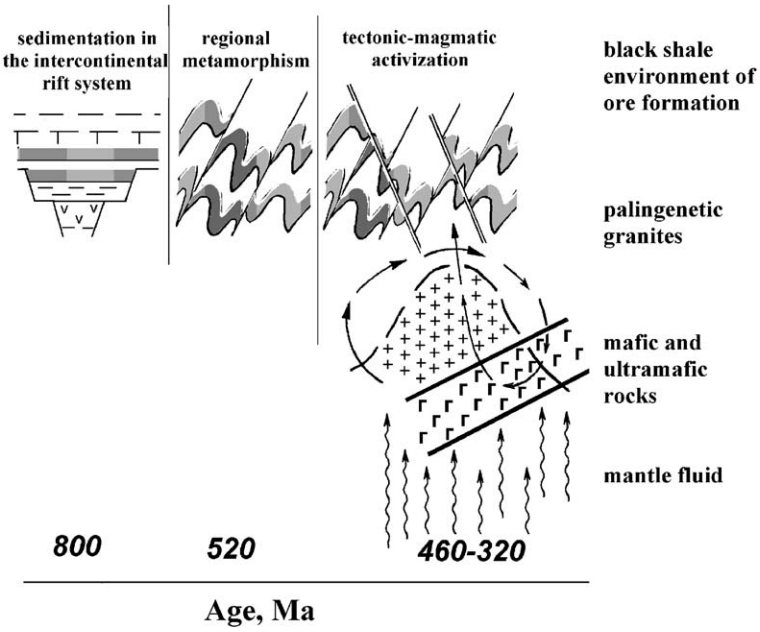

Fig. 22. Genetic model for Sukhoi Log Pt–Au mineralization (see text).

The evolution of redox conditions due to changes in the solution acidity can cause disproportionation reactions such as:

$$2PtCl_2 = Pt^o + PtCl_4$$

which could be a major cause of native metal precipitation (Distler et al., 2000) as has been shown for active high-temperature fumaroles (Distler et al., 2002). The Pt–Cu disordered solid solutions are the most abundant intermetallics both in the Sukhoi Log and the Waterberg deposits.

The main events for the Sukhoi Log deposit have been dated isotopically (Laverov et al., 2000c). The terrigenous host strata were deposited during the Early to Middle Riphean (about 800 Ma) and were metamorphosed at 516 ± 22 Ma. The age of the mineralization was determined on quartz separates by the Rb–Sr method at 320 ± 16 Ma. Similar values (350–370 Ma) were obtained by isotopic dating of the granitoid massifs of the Bodaibo synclinorium and correspond to a period of tectonomagmatic reactivation and granite formation.

Isotopic compositions of galena show that the lead evolved in a source with U/Pb ratio similar to the average crustal value ($\mu_2 = 9.6$), and the model Pb–Pb age is 380–400 Ma (Stacey-Kramers model). Therefore, mineralization is much younger than sedimentation and regional metamorphism. Based on these data, as well as the results of geophysical modeling of the deep structure of the Sukhoi Log deposit, we have constructed a general model of Pt–Au mineralization (Fig. 22). The main factor controlling this process was the tectonic regime of the Early–Middle Paleozoic reactivation and the associated endogenous fluid flux. This resulted in palingenetic granite formation and mobilization of ore components from a vast volume of the Early Precambrian basement and ancient ultramafic rocks as well as from upper crustal rocks including carbon-bearing terrigenous rocks. The combination of regional events in an extensive sedimentary basin superimposed on the mafic–ultramafic belt and local intrusion of granite determined the unique composition and structure of the deposit, as well as its immense concentration of precious metals.

Acknowledgements

The research was realized through funding from Russian Academy of Sciences, Russian Foundation of Basic Research (grants 98-05-64775 and 00-05-64378), Federal Program "Integracia" (project I-0640), Science Support Foundation, Ministry of Natural Resources, Ministry of Industry and Science of Russia, as well as the Lenzoloto Company. The encouragement of Academician N.P. Laverov and member-correspondents of RAS Yu.G. Safonov and I.V. Chernyshov are gratefully acknowledged. We are grateful to many colleagues for helpful discussions. We thank I.B. Nikitina, N.N. Nikolskaya, S.A. Gorbacheva, V.A. Sychkova, G.E. Belousov, M.V. Kuznetsova for chemical analyses, and Andrey V. Mokhov for electron microscope study. We are most grateful to C. Stanley for excellent editing of English of our manuscript. The authors particularly thank J. Pašava, R.M. Coveney, and reviewers of journal for their valuable comments on the manuscript.

References

Alakshin, A.M., Pismennyi, B.M., 1988. O stroenii zemnoi kory zony sochleneniya Sibirskoi platformy so skladchatym obramleniem. Geol. Geophys. 11, 24–31 (in Russian).

Barton, P.B., Toulmin, P., 1966. Phase relation involving sphalerite in the Fe–Zn–S system. Econ. Geol. 61, 815–849.

Bau, M., 1991. Rare-earth elements mobility during hydrothermal and metamorphic fluid–rock interaction and the significance of the oxidation state of europium. Chem. Geol. 93, 219–230.

Bierlein, F.P., Crow, D.E., 2000. Phanerozoic orogenic lode gold deposits. In: Hagemann, S.G., Brown, P.E. (Eds.), Gold in 2000. Society of Economic Geologists. Reviews in Economic Geology, vol. 13, pp. 103–139.

Bodnar, R.J., Vityk, M.O., 1994. Interpretation of microthermometric data for H_2O–NaCl fluid inclusions. In: De Vivo, B., Frezzotti, M.L. (Eds.), Fluid inclusions in Minerals: Methods and Applications. Pontignano-Siena, Lissabon, pp. 117–130.

Bottinga, Y., 1969. Calculated fractionation factors for carbon and hydrogen isotope exchange in the system calcite–carbon dioxide–graphite, methane–hydrogen–water vapor. Geochim. Cosmochim. Acta 33, 49–64.

Brown, P.E., 1989. FLINCOR: a fluid inclusion data reduction and exploration program. Second Biennial Pan-American Conf. on Research on Fluid Inclusions Prog. with Abstr., p. 14.

Brown, P.E., Lamb, W.M., 1989. P–V–T properties of fluids in the system $H_2O \pm CO_2 \pm$ NaCl: new graphical presentations and implications for fluid inclusion studies. Geochim. Cosmochim. Acta 53, 1209–1222.

Buryak, V.A., Khmelevskaya, N.M., 1997. Sukhoi Log-odno iz krupneishikh zolotorudnysh mestorojdenii mira. Dalnauka, Vladivostok.

Gammons, C.H., 1995. Experimental investigations of the hydrothermal geochemistry of platinum and palladium. Geochim. Cosmochim. Acta 59, 1655–1669.

Gammons, C.N., Williams-Jones, A.E., 1997. Chemical mobility of gold in the porphyry-epithermal environment. Econ. Geol. 92, 45–59.

Cabri, L.J., Campbell, J.L., Laflomme, J.H.G., Leigh, R.G., Maxwell, J.A., Scott, J.D., 1985. Proton-microprobe analysis of trace elements in sulfides from massive sulfide deposits. Can. Mineral. 23, 133–148.

Carothers, W.W., Adami, L.H., Rosenbauer, R.J., 1988. Experimental oxygen isotope fractionation between siderite–water and phosphoric acid liberated CO_2–siderite. Geochim. Cosmochim. Acta 52, 2445–2450.

Claypool, G.M., Kaplan, J.R., 1974. The origin and distribution of methane in marine sediments. Natural Gases in Marine Sediments, vol. 3. Plenum, New York, p. 132.

Collins, P.L.P., 1979. Gas hydrates in CO_2-bearing fluid inclusions and the use of freezing data for estimation of salinity. Econ. Geol. 74, 1435–1444.

Coveney Jr., R.M., Murowchick, J.B., Grauch, R.I., Glascock, M.D., Denison, J.R. 1992. Gold and platinum in shales with evidence against extraterrestrial sources of metals. Chem. Geol. 99, 101–114.

Darling, R.S., 1991. An extended equation to calculate NaCl contents from final clathrate melting temperatures in H_2O–CO_2–NaCl fluid inclusions: implications for P–T–isochore location. Geochim. Cosmochim. Acta 55, 3869–3871.

Distler, V.V., Grokhovskaya, T.L., Evstigneeva, T.L., Sluzhenikin, S.F., Dyuzhikov, O.A., 1988. Petrologiya magmaticheskogo sulfidnogo rudoobrazovaniya. Nauka, Moscow. In Russian.

Distler, V.V., Mitrofanov, G.L., Nemerov, V.K., Kovalenker, V.A., Mokhov, A.V., Semeykina, L.K., Yudovskaya, M.A., 1996. Phormy nakhozhdeniya metallov platinovoy gruppy I ikh genesis v zolotorudnom mestorozhdenii Sukhoy Log (Rossiya). Geol. Rudn. Mestorozd. 38, 467–484 (in Russian).

Distler, V.V., Sluzhenikin, S.F., Cabri, L.J., Krivolutskaya, N.A., Turovtsev, D.M., Golovanova, T.A., Mokhov, A.V., Knauf, V.V., Oleshkevich, O.I., 1999. Platinum ores of the Norilsk Layered intrusions: magmatic and fluid concentration of noble metals. Geology of Ore Deposits, vol. 41 (3). Nauka/Interperiodica, Moscow, pp. 214–237.

Distler, V.V., Yudovskaya, M.A., Prokof'ev, V.Yu., Sluzhenikin, S.F., Mokhov, A.V., Mun, Y.A.V., 2000. Hydrothermal platinum mineralization of the Waterberg deposit (Transvaal, South Africa). Geology of Ore Deposits, vol. 42 (4). Nauka/Interperiodica, Russia, pp. 328–339.

Distler, V.V., Yudovskaya, M.A., Znamensky, V.S., Chaplygin, I.V., 2002. Platinum group elements in the active fumaroles of Kudryavyi volcano (Iturup Island, the Kuril Island Arc). Dokl. Earth Sci. 387 (8), 975–979.

Douville, E., Bienvenu, P., Charlou, J.L., Donval, J.P., Fouquet, Y., Appriou, P., Gamo, T., 1999. Yttrium and rare earth elements in fluids from various deep-sea hydrothermal systems. Geochim. Cosmochim. Acta 63, 627–643.

Faure, G., 1986. Principles of Isotope Geology, 2nd ed. Wiley.

Genkin, A.D., Bortnikov, N.S., Cabri, L.J., Wagner, F.E., Stanley, C.J., Safonov, Y.G., McMahon, G., Friedl, J., Kerzin, A.L., Gamyanin, G.N., 1998. A multidisciplinary study of invisible gold in arsenopyrite from four mesothermal gold deposits in Siberia, Russian Federation. Econ. Geol. 93, 463–487.

Gize, A.P., 1999. A special issue on organic matter and ore deposits: interactions, applications, and case studies (Introduction). Econ. Geol. 94, 963–966.

Juvonen, M.-R., Lakomaa, T.M., Kallio, E.I., 2000. The nickel sulfide fire assay procedure for different types of rocks in the determination of gold and the platinum group elements by inductively coupled plasma-mass spectrometry. Abstracts of 31st International Geological Congress. Rio de Janeiro, Brasil.

Kalyuzhny, V.A., 1982. Osnovy ucheniya o mineraloobrazuyuschikh fluidakh. Naukova Dumka, Kiev. In Russian.

Kerkhof, A.M., 1988. The System CO_2–CH_4–N_2 in Fluid Inclusions: Theoretical Modeling Geological Applications. Free Univ. Press, Amsterdam.

Khamrabaev, I.Kh., Zuev, U.N., Azimov, P.T., Sidorova, I.P., 1995. Skrytyi Muruntauskii granitoidnyi intrusiv (po dannym Muruntauskoi sverkh-glubokoi skvajiny SG-10). Uzb. Geol. J. 4, 45–59 (in Russian).

Kucha, H., 1982. Platinum Group metals in the Zechstein copper deposits. Pol. Econ. Geol. 77, 1578–1591.

Laverov, N.P., Lishnevskii, E.N., Distler, V.V., Tchernov, A.A., 2000a. Model rudno-magmaticheskoi sistemy zoloto-platinovogo mestorojdeniya Sukhoi Log, Vostochnaya Sibir, Rossia. Dokl. Earth Sci. 375, 652–656 (in Russian).

Laverov, N.P., Prokof'ev, V.Yu., Distler, V.V., Yudovskaya, M.A., Spiridonov, A.M., Grebenshchikova, V.I., Matel, N.L., 2000b. New data on conditions of ore deposition and composition of ore-forming fluids in the Sukhoi Log gold–platinum deposit. Dokl. Earth Sci. 371 (2), 357–361.

Laverov, N.P., Chernyshov, I.V., Distler, V.V., Bairova, E.D., Golzman, Yu.V., Golubev, V.N., Chugaev, A.V., Yudovskaya, M.A., 2000c. Geokhronologiya i vozmoznye istochniki rudnogo veschestva mestorojdeniya Sukhoi Log: rezultaty izotopnykh issledovanii. Izotopnoe datirovanie geologicheskikh prozessov: novye metody i resultaty. Geos, Moscow, pp. 211–214.

McDonald, I., Vaughan, D.J., Tredoux, M., 1995. Platinum mineralization in quartz veins near Nabumspruit, central Transvaal. S. Afr. Tydskr. Geol. 98 (2), 168–175.

Mishenkin, B.P., Krupskaya, G.V., Petric, G.V., Seleznev, V.S., 1975. Glubinnye seismicheskie issledovaniya na Severo-vostoke Baikalskoi riftovoi zony. Geol. Geophys. 4, 71–78 (in Russian).

Mitrofanov, G.L., Nemerov, V.K., Korobeinikov, N.K., Semeikina, L.K., 1994. Platinonosnyi potencial pozdnedokembriiskish uglerodistysh formacii Baikalo-Patomskogo nagor'ya. *Platina Rossii*. Problemy razvitiya mineral syr'evoi bazy platinovykh metallov. Geoinformmark, Moscow, pp. 150–154. In Russian.

Morgan, J.W., Wandless, G.A., 1980. Rare earth elements in some hydrothermal minerals: evidence for crystallographic control. Geochim. Cosmochim. Acta 44, 973–980.

Pašava, J., 1993. Anoxic sediments—an important environment for PGE; an overview. Ore Geol. Rev. 8, 425–445.

Razvozzhaeva, E.A., Prokof'ev, V.Yu., Spiridonov, A.M., Martikhaev, D.Kh., Prokopchuk, S.I., 2002. Precious metals and carbonaceous substance in ores of the Sukhoi Log deposit (Eastern Siberia, Russia). Geol. Ore Depos. 44 (2), 103–111.

Roedder, E., 1984. Fluid inclusions. Review in Mineralogy, vol. 12. Mineralogical Society of America, Washington.

Ronov, A.B., Migdisov, A.A., 1971. Geochemical history of the crystalline basement and the sedimentary cover of the Russian and North American Platforms. Sedimentology 16, 167–185.

Rundqist, I.K., Bobrov, V.A., Smirnova, T.N., Cmirnov, M.Y., Danilova, M.Y., Ascheulov, A.A., 1992. Etapy formirovaniya Bodaibinskogo zolotorudnogo raiona. Geol. Rudn. Mestorozd. 34, 3–15 (in Russian).

Symonds, R.B., Reed, M.H., 1993. Calculation of multicomponent chemical equilibrium in gas solid liquid systems: calculation methods, thermochemical data and applications to studies of high-temperature volcanic gases with examples from Mount St. Helens. Am. J. Sci. 293, 758–864.

Taylor, H.P., McLennan, S.M., 1985. The Continental Crust: Its Composition and Evolution. Blackwell, Oxford.

Thiery, R., Kerkhof, A.M, Dubessy, J., 1994. PTX properties of CH_4-CO_2 and CO_2-N_2 fluid inclusions: modeling for $T<31$ °C and $P<400$ bars. Eur. J. Mineral. 6, 753–771.

Van der Flier-Keller, E., 1991. Platinum group elements in Tulameen Coal, British Columbia, Canada. Econ. Geol. 86, 387–395.

Varshal, G.M., Velyukhanova, T.K., Koshcheeva, I.Y., Baranova, N.N., Koserenko, S.V., 1994. Koncentrirovanie blagorodnysh metallov yglerodistym beschestvom. Geokhimiya 6, 814–823 (in Russian).

Vikulova, P.P., Serova, N.L., Novikova, A.N., 1977. Kombinaziya metodov izucheniya pirita na zolotom mestorozdenii v Vostochnoi Sibiri. Novye metody analiza. Vostsibniigims, Irkutsk, pp. 46–54. In Russian.

Vysotskii, N.K., 1933. Platina i raiony ee dobychi. Izdatelstvo Akademii Nauk SSSR, Leningrad. In Russian.

Watanabe, Y., Haraoka, H., Wronkiewicz, C., Condie, K.C., Ohmoto, H., 1997. Carbon, nitrogen, and sulfur geochemistry of Archean and Proterozoic shales from the Kaapvaal Craton, South Africa. Geochim. Cosmochim. Acta 61, 3441–3460.